

Refractive index less than two: photonic nanojets yesterday, today and tomorrow [Invited]

BORIS S. LUK'YANCHUK,^{1,2,3,*} RAMÓN PANIAGUA-DOMÍNGUEZ,¹ IGOR MININ,⁴ OLEG MININ,⁵ AND ZENGBO WANG⁶

¹Data Storage Institute, A*STAR (Agency for Science, Technology and Research), 2 Fusionopolis Way, Kinesis, 138634, Singapore

²Division of Physics and Applied Physics, School of Physical and Mathematical Sciences, Nanyang Technological University, 637371 Singapore

³Faculty of Physics, Lomonosov Moscow State University, Moscow 119991, Russia

⁴Tomsk Polytechnic University, 36, Lenin Avenue, 634050, Russia

⁵Tomsk State University, Tomsk, 30 Lenin Avenue, 634050, Russia

⁶School of Electronic Engineering, Bangor University, Bangor LL57 1UT, UK

*Boris_L@dsi.a-star.edu.sg

Abstract: Materials with relatively small refractive indices ($n < 2$), such as glass, quartz, polymers, some ceramics, etc., are the basic materials in most optical components (lenses, optical fibres, etc.). In this review, we present some of the phenomena and possible applications arising from the interaction of light with particles with a refractive index less than 2. The vast majority of the physics involved can be described with the help of the exact, analytical solution of Maxwell's equations for spherical particles (so called Mie theory). We also discuss some other particle geometries (spheroidal, cubic, etc.) and different particle configurations (isolated or interacting) and draw an overview of the possible applications of such materials, in connection with field enhancement and super resolution nanoscopy.

© 2017 Optical Society of America

OCIS codes: (100.6640) Superresolution; (180.4243) Near-field microscopy; (290.4020) Mie theory; (350.3950) Micro-optics; (350.4990) Particles.

References and links

1. A. Kwan, J. Dudley, and E. Lantz, "Who really discovered Snell's law?" *Phys. World* **15**(4), 64 (2002).
2. V. I. Arnold, "On teaching mathematics," *Russ. Math. Surv.* **53**(1), 229–236 (1998).
3. B. Luk'yanchuk, N. Arnold, S. M. Huang, Z. B. Wang, and M. H. Hong, "Three-dimensional effects in dry laser cleaning," *Appl. Phys., A Mater. Sci. Process.* **77**, 209–215 (2003).
4. L. Rayleigh, "On the light from the sky, its polarization and colour," *Phil. Mag.* Vol. **41**, 447–454 (1871).
5. C. F. Bohren and D. R. Huffman, *Absorption and Scattering of Light by Small Particles* (Wiley, 1998).
6. B. Luk'yanchuk, Y. W. Zheng, and Y. F. Lu, "Laser cleaning of solid surface: Optical resonance and near-field effects," *Proc. SPIE*, **4065**, 576–587 (2000).
7. H. J. Münzer, M. Mosbacher, M. Bertsch, J. Zimmermann, P. Leiderer, and J. Boneberg, "Local field enhancement effects for nanostructuring of surfaces," *J. Microsc.* **202**(Pt 1), 129–135 (2001).
8. M. Mosbacher, H.-J. Münzer, J. Zimmermann, J. Solis, J. Boneberg, and P. Leiderer, "Optical field enhancement effects in laser-assisted particle removal," *Appl. Phys., A Mater. Sci. Process.* **72**(1), 41–44 (2001).
9. Y. W. Zheng, B. S. Luk'yanchuk, Y. F. Lu, W. D. Song, and Z. H. Mai, "Dry laser cleaning of particles from solid substrates: experiments and theory," *J. Appl. Phys.* **90**(5), 2135–2142 (2001).
10. B. Luk'yanchuk, ed., *Laser Cleaning* (World Scientific, 2002).
11. Y. F. Lu, L. Zhang, W. D. Song, Y. W. Zheng, and B. S. Luk'yanchuk, "Laser writing of a subwavelength structure on silicon (100) surfaces with particle enhanced optical irradiation," *JETP Lett.* **72**(9), 457–459 (2000).
12. P. Leiderer, C. Bartels, J. König-Birk, M. Mosbacher, and J. Boneberg, "Imaging optical near-fields of nanostructures," *Appl. Phys. Lett.* **85**(22), 5370–5372 (2004).
13. S. M. Huang, M. H. Hong, Y. F. Lu, B. S. Luk'yanchuk, W. D. Song, and T. C. Chong, "Pulsed laser-assisted surface structuring with optical near-field enhanced effects," *J. Appl. Phys.* **92**(5), 2495–2500 (2002).
14. K. Piglmayer, R. Denk, and D. Bäuerle, "Laser-induced surface patterning by means of microspheres," *Appl. Phys. Lett.* **80**(25), 4693–4695 (2002).

15. N. Chaoui, J. Solis, C. N. Afonso, T. Fourier, T. Muehlberger, G. Schrems, M. Mosbacher, D. Bäuerle, M. Bertsch, and P. Leiderer, "A high-sensitivity in situ optical diagnostic technique for laser cleaning of transparent substrates," *Appl. Phys., A Mater. Sci. Process.* **76**(5), 767–771 (2003).
16. P. Leiderer, C. Bartels, J. König-Birk, M. Mosbacher, and J. Boneberg, "Imaging optical near-fields of nanostructures," *Appl. Phys. Lett.* **85**(22), 5370–5372 (2004).
17. B. S. Luk'yanchuk, Z. B. Wang, W. D. Song, and M. H. Hong, "Particle on surface: 3D - effects in dry laser cleaning," *Appl. Phys., A Mater. Sci. Process.* **79**(4-6), 747–751 (2004).
18. J. Kofler and N. Arnold, "Axially symmetric focusing as a cuspid diffraction catastrophe: Scalar and vector cases and comparison with the theory of Mie," *Phys. Rev. B* **73**(23), 235401 (2006).
19. Y. A. Kravtsov and Y. I. Orlov, *Geometrical Optics of Inhomogeneous Media* (Springer, Berlin 1990).
20. M. V. Berry and C. Upstill, "Catastrophe optics: Morphologies of caustics and their diffraction pattern," In *Progress in Optics*, Vol. **18**, 259–346, ed. by E. Wolf (Elsevier, North-Holland 1980).
21. Z. Chen, A. Taflove, and V. Backman, "Photonic nanojet enhancement of backscattering of light by nanoparticles: a potential novel visible-light ultramicroscopy technique," *Opt. Express* **12**(7), 1214–1220 (2004).
22. X. Li, Z. Chen, A. Taflove, and V. Backman, "Optical analysis of nanoparticles via enhanced backscattering facilitated by 3-D photonic nanojets," *Opt. Express* **13**(2), 526–533 (2005).
23. X. Li, Z. G. Chen, M. P. Siegel, A. Taflove, and V. Backman, "Analysis of nanoparticles using photonic nanojet," *Proc. SPIE* **5705**, 14–22 (2005).
24. Z. Chen, A. Taflove, X. Li, and V. Backman, "Superenhanced backscattering of light by nanoparticles," *Opt. Lett.* **31**(2), 196–198 (2006).
25. Z. Chen, X. Li, A. Taflove, and V. Backman, "Backscattering enhancement of light by nanoparticles positioned in localized optical intensity peaks," *Appl. Opt.* **45**(4), 633–638 (2006).
26. A. Heifetz, K. Huang, A. V. Sahakian, X. Li, A. Taflove, and V. Backman, "Experimental confirmation of backscattering enhancement induced by a photonic jet," *Appl. Phys. Lett.* **89**(22), 221118 (2006).
27. S.-C. Kong, A. Sahakian, A. Heifetz, A. Taflove, and V. Backman, "Robust detection of deeply subwavelength pits in simulated optical data-storage disks using photonic jets," *Appl. Phys. Lett.* **92**(21), 211102 (2008).
28. A. Heifetz, S. C. Kong, A. V. Sahakian, A. Taflove, and V. Backman, "Photonic Nanojets," *J. Comput. Theor. Nanosci.* **6**(9), 1979–1992 (2009).
29. S. Yang, A. Taflove, and V. Backman, "Experimental confirmation at visible light wavelengths of the backscattering enhancement phenomenon of the photonic nanojet," *Opt. Express* **19**(8), 7084–7093 (2011).
30. V. N. Astratov, J. P. Franchak, and S. P. Ashili, "Optical coupling and transport phenomena in chains of spherical dielectric microresonators with size disorder," *Appl. Phys. Lett.* **85**(23), 5508–5510 (2004).
31. G. Kattawar, C. Li, P. W. Zhai, and P. Yang, "Electric and magnetic energy density distributions inside and outside dielectric particles illuminated by a plane electromagnetic wave," *Opt. Express* **13**(12), 4554–4559 (2005).
32. S. Lecler, Y. Takakura, and P. Meyrueis, "Properties of a three-dimensional photonic jet," *Opt. Lett.* **30**(19), 2641–2643 (2005).
33. A. V. Itagi and W. A. Challener, "Optics of photonic nanojets," *J. Opt. Soc. Am. A* **22**(12), 2847–2858 (2005).
34. A. V. Kanaev, V. N. Astratov, and W. Cai, "Optical coupling at a distance between detuned spherical cavities," *Appl. Phys. Lett.* **88**(11), 111111 (2006).
35. A. M. Kapitonov and V. N. Astratov, "Observation of nanojet-induced modes with small propagation losses in chains of coupled spherical cavities," *Opt. Lett.* **32**(4), 409–411 (2007).
36. K. J. Yi, H. Wang, Y. F. Lu, and Z. Y. Yang, "Enhanced Raman scattering by self-assembled silica spherical Microparticles," *J. Appl. Phys.* **101**(6), 063528 (2007).
37. S. Lecler, S. Haacke, N. Lecong, O. Crégut, J.-L. Rehspringer, and C. Hirlimann, "Photonic jet driven non-linear optics: example of two-photon fluorescence enhancement by dielectric microspheres," *Opt. Express* **15**(8), 4935–4942 (2007).
38. Z. B. Wang, W. Guo, A. Pena, D. J. Whitehead, B. S. Luk'yanchuk, L. Li, Z. Liu, Y. Zhou, and M. H. Hong, "Laser micro/nano fabrication in glass with tunable-focus particle lens array," *Opt. Express* **16**(24), 19706–19711 (2008).
39. S.-C. Kong, A. Sahakian, A. Taflove, and V. Backman, "Photonic nanojet-enabled optical data storage," *Opt. Express* **16**(18), 13713–13719 (2008).
40. E. McLeod and C. B. Arnold, "Subwavelength direct-write nanopatterning using optically trapped microspheres," *Nat. Nanotechnol.* **3**(7), 413–417 (2008).
41. S. Yang and V. N. Astratov, "Photonic nanojet-induced modes in chains of size-disordered microspheres with an attenuation of only 0.08 dB per sphere," *Appl. Phys. Lett.* **92**(26), 261111 (2008).
42. A. Devilez, B. Stout, N. Bonod, and E. Popov, "Spectral analysis of three-dimensional photonic jets," *Opt. Express* **16**(18), 14200–14212 (2008).
43. P. Ferrand, J. Wenger, A. Devilez, M. Pianta, B. Stout, N. Bonod, E. Popov, and H. Rigneault, "Direct imaging of photonic nanojets," *Opt. Express* **16**(10), 6930–6940 (2008).
44. L. Zhao and C. K. Ong, "Direct observation of photonic jets and corresponding backscattering enhancement at microwave frequencies," *J. Appl. Phys.* **105**(12), 123512 (2009).
45. K. Holms, B. Hourahine, and F. Papoff, "Calculation of internal and scattered fields of axisymmetric nanoparticles at any point in space," *J. Opt. A, Pure Appl. Opt.* **11**(5), 054009 (2009).

46. C. M. Ruiz and J. J. Simpson, "Detection of embedded ultra-subwavelength-thin dielectric features using elongated photonic nanojets," *Opt. Express* **18**(16), 16805–16812 (2010).
47. T. Wang, C. Kuang, X. Hao, and X. Liu, "Subwavelength focusing by a microsphere array," *J. Opt.* **13**(3), 035702 (2011).
48. S. Yang, A. Taflove, and V. Backman, "Experimental confirmation at visible light wavelengths of the backscattering enhancement phenomenon of the photonic nanojet," *Opt. Express* **19**(8), 7084–7093 (2011).
49. A. Darafshah and V. N. Astratov, "Periodically focused modes in chains of dielectric spheres," *Appl. Phys. Lett.* **100**(6), 061123 (2012).
50. Z. B. Wang, Z. Yi, and B. Luk'yanchuk, "Near-field focusing of dielectric microspheres: Super-resolution and field-invariant parameter scaling," arXiv:1304.4139 (2013).
51. H. Guo, Y. Han, X. Weng, Y. Zhao, G. Sui, Y. Wang, and S. Zhuang, "Near-field focusing of the dielectric microsphere with wavelength scale radius," *Opt. Express* **21**(2), 2434–2443 (2013).
52. C.-Y. Liu and Y. Wang, "Real-space observation of photonic nanojet in microspheres," *Physica E* **61**, 141–147 (2014).
53. C.-Y. Liu, "Ultra-high transmission of photonic nanojet induced modes in chains of core-shell microcylinders," *Phys. Lett. A* **376**(45), 3261–3266 (2012).
54. C.-Y. Liu, "Superenhanced photonic nanojet by core-shell microcylinders," *Phys. Lett. A* **376**(23), 1856–1860 (2012).
55. Y. Takakura, H. Halaq, S. Lecler, S. Robert, and B. Sauviac, "Single and dual photonic jets with tipped waveguides: An integral approach," *IEEE Photonics Technol. Lett.* **24**(17), 1516–1518 (2012).
56. C.-Y. Liu, "Tunable photonic nanojet achieved by core-shell microcylinder with nematic liquid crystal," *J. Mod. Opt.* **60**(7), 538–543 (2013).
57. B. Ounnas, B. Sauviac, Y. Takakura, S. Lecler, B. Bayard, and S. Robert, "Single and Dual Photonic Jets and Corresponding Backscattering Enhancement With Tipped Waveguides: Direct Observation at Microwave Frequencies," *IEEE Trans. Antenn. Propag.* **63**(12), 5612–5618 (2015).
58. M. Guo, Y. H. Ye, J. Hou, and B. Du, "Experimental far-field imaging properties of high refractive index microsphere lens," *Photonics Research* **3**(6), 339–342 (2015).
59. C.-Y. Liu and K.-L. Hsiao, "Direct imaging of optimal photonic nanojets from core-shell microcylinders," *Opt. Lett.* **40**(22), 5303–5306 (2015).
60. M. Kerker, D.-S. Wang, and C.-L. Giles, "Electromagnetic scattering by magnetic spheres," *J. Opt. Soc. Am.* **73**(6), 765–767 (1983).
61. M. Nieto-Vesperinas, R. Gómez-Medina, and J. J. Sáenz, "Angle-suppressed scattering and optical forces on submicrometer dielectric particles," *J. Opt. Soc. Am. A* **28**(1), 54–60 (2011).
62. B. Luk'yanchuk, N. Voshchinnikov, R. Paniagua-Dominguez, and A. Kuznetsov, "Optimum Forward Light Scattering by Spherical and Spheroidal Dielectric Nanoparticles with High Refractive Index," *ACS Photonics* **2**(7), 993–999 (2015).
63. Y. Zhang, M. Nieto-Vesperinas, and J. J. Sáenz, "Dielectric spheres with maximum forward scattering and zero backscattering: a search for their material composition," *J. Opt.* **17**(10), 105612 (2015).
64. B. Luk'yanchuk, N. I. Zheludev, S. A. Maier, N. J. Halas, P. Nordlander, H. Giessen, and C. T. Chong, "The Fano resonance in plasmonic nanostructures and metamaterials," *Nat. Mater.* **9**(9), 707–715 (2010).
65. P. W. Barber and S. C. Hill, *Light Scattering by Particles: Computational Methods* (World Scientific, 1990).
66. P. Albella, M. A. Poyli, M. K. Schmidt, S. A. Maier, F. Moreno, J. J. Sáenz, and J. Aizpurua, "Low-Loss Electric and Magnetic Field-Enhanced Spectroscopy with Subwavelength Silicon Dimers," *J. Phys. Chem. C* **117**(26), 13573–13584 (2013).
67. R. M. Bakker, D. Permyakov, Y. F. Yu, D. Markovich, R. Paniagua-Dominguez, L. Gonzaga, A. Samusev, Y. Kivshar, B. Luk'yanchuk, and A. I. Kuznetsov, "Magnetic and electric hotspots with silicon nanodimers," *Nano Lett.* **15**(3), 2137–2142 (2015).
68. D. G. Baranov, R. S. Savelev, S. V. Li, A. E. Krasnok, and A. Alu, "Modifying magnetic dipole spontaneous emission with nanophotonic structures," *Laser Photonics Rev.* **2017**, 1600268 (2017).
69. M. Born and E. Wolf, *Principles of Optics*, 7th ed. (Cambridge University Press, 1999).
70. T. R. M. Sales, "Smallest Focal Spot," *Phys. Rev. Lett.* **81**(18), 3844–3847 (1998).
71. J. F. Nye, "Evolution from a Fraunhofer to a Pearcey diffraction pattern," *J. Opt. A, Pure Appl. Opt.* **5**(5), 495–502 (2003).
72. W. Zolowich, "Light rays and imaging in wave optics," *Phys. Rev. E* **64**, 066 610 (2001).
73. P. A. Bobbert and J. Vliieger, "Light scattering by a sphere on a substrate," *Physica A* **137**(1-2), 209–242 (1986).
74. D. Bedeaux, and J. Vliieger, *Optical Properties of Surfaces* (Imperial College Press, 2004).
75. Z. Wang, W. Guo, L. Li, B. Luk'yanchuk, A. Khan, Z. Liu, Z. Chen, and M. Hong, "Optical virtual imaging at 50 nm lateral resolution with a white-light nanoscope," *Nat. Commun.* **2**, 218 (2011).
76. C.-Y. Liu and C.-C. Li, "Photonic nanojet induced modes generated by a chain of dielectric microdisks," *Optik (Stuttg.)* **127**(1), 267–273 (2016).
77. L. Han, Y. Han, J. Wang, G. Gouesbet, and G. Gréhan, "Controllable and enhanced photonic jet generated by fiber combined with spheroid," *Opt. Lett.* **39**(6), 1585–1588 (2014).
78. V. Pacheco-Peña, M. Beruete, I. V. Minin, and O. V. Minin, "Terajets produced by 3D dielectric cuboids," *Appl. Phys. Lett.* **105**(8), 084102 (2014).

79. I. V. Minin, O. V. Minin, and Y. E. Geintz, "Localized EM and photonic jets from non-spherical and non-symmetrical dielectric mesoscale objects: brief review," *Ann. Phys.* **527**(7–8), 491–497 (2015).
80. Yu. E. Geintz, A. A. Zemlyanov, and E. K. Panina, "Photonic Nanonojets from Nonspherical Dielectric Microparticles," *Russ. Phys. J.* **58**(7), 904–910 (2015).
81. Yu. E. Geints, A. A. Zemlyanov, and E. K. Panina, "Characteristics of photonic jets from microcones," *Opt. Spectrosc.* **119**(5), 849–854 (2015).
82. P. Wu, J. Li, K. Wei, and W. Yue, "Tunable and ultra-elongated photonic nanojet generated by a liquid-immersed core-shell dielectric microsphere," *Appl. Phys. Express* **8**(11), 112001 (2015).
83. I. V. Minin, O. V. Minin, and N. A. Kharitoshin, "Localized high field enhancements from hemispherical 3D mesoscale dielectric particles in the reflection mode," *Proc. 16th International Conference of Young Specialists on Micro/Nanotechnologies and Electron Devices, IEEE*, June 29, 331–333 (2015).
84. I. Minin and O. Minin, *Diffraction Optics and Nanophotonics: Resolution below the Diffraction Limit* (Springer, 2016).
85. I. V. Minin, O. V. Minin, V. Pacheco-Peña, and M. Beruete, "Subwavelength optical trap in the field of a standing wave on photonic jets," *Quantum Electron.* **46**, 555–557 (2016).
86. I. V. Minin, O. V. Minin, V. Pacheco-Peña, and M. Beruete, "Localized photonic jets from flat, three-dimensional dielectric cuboids in the reflection mode," *Opt. Lett.* **40**(10), 2329–2332 (2015).
87. M. X. Wu, B. J. Huang, R. Chen, Y. Yang, J. F. Wu, R. Ji, X. D. Chen, and M. H. Hong, "Modulation of photonic nanojets generated by microspheres decorated with concentric rings," *Opt. Express* **23**(15), 20096–20103 (2015).
88. B. Yan, L. Y. Yue, and Z. B. Wang, "Engineering near-field focusing of a microsphere lens with pupil masks," *Opt. Commun.* **370**, 140–144 (2016).
89. M. Wu, R. Chen, J. Soh, Y. Shen, L. Jiao, J. Wu, X. Chen, R. Ji, and M. Hong, "Super-focusing of center-covered engineered microsphere," *Sci. Rep.* **6**(1), 31637 (2016).
90. L. Yue, B. Yan, and Z. Wang, "Photonic nanojet of cylindrical metalens assembled by hexagonally arranged nanofibers for breaking the diffraction limit," *Opt. Lett.* **41**(7), 1336–1339 (2016).
91. E. Betzig, J. K. Trautman, T. D. Harris, J. S. Weiner, and R. L. Kostelak, "Breaking the diffraction barrier: optical microscopy on a nanometric scale," *Science* **251**(5000), 1468–1470 (1991).
92. J. Y. Lee, B. H. Hong, W. Y. Kim, S. K. Min, Y. Kim, M. V. Jouravlev, R. Bose, K. S. Kim, I.-C. Hwang, L. J. Kaufman, C. W. Wong, P. Kim, and K. S. Kim, "Near-field focusing and magnification through self-assembled nanoscale spherical lenses," *Nature* **460**(7254), 498–501 (2009).
93. X. Hao, C. Kuang, X. Liu, H. Zhang, and Y. Li, "Microsphere based microscope with optical super-resolution capability," *Appl. Phys. Lett.* **99**(20), 203102 (2011).
94. G. F. W. Darafsheh, L. D. Negro, and V. N. Astratov, "Optical super-resolution by high-index liquid-immersed microspheres," *Appl. Phys. Lett.* **101**(14), 141128 (2012).
95. L. A. Krivitsky, J. J. Wang, Z. Wang, and B. Luk'yanchuk, "Locomotion of microspheres for super-resolution imaging," *Sci. Rep.* **3**(1), 3501 (2013).
96. L. Li, W. Guo, Y. Yan, S. Lee, and T. Wang, "Label-free super-resolution imaging of adenoviruses by submerged microsphere optical nanoscopy," *Light Sci. Appl.* **2**(9), e104 (2013).
97. X. Hao, C. Kuang, Z. Gu, Y. Wang, S. Li, Y. Ku, Y. Li, J. Ge, and X. Liu, "From microscopy to nanoscopy via visible light," *Light Sci. Appl.* **2**(10), e108 (2013).
98. H. Guo, Y. Han, X. Weng, Y. Zhao, G. Sui, Y. Wang, and S. Zhuang, "Near-field focusing of the dielectric microsphere with wavelength scale radius," *Opt. Express* **21**(2), 2434–2443 (2013).
99. S. Lee, L. Li, Y. Ben-Aryeh, Z. Wang, and W. Guo, "Overcoming the diffraction limit induced by microsphere optical nanoscopy," *J. Opt.* **15**(12), 125710 (2013).
100. X. Hao, C. Kuang, Y. Li, and X. Liu, "Evanescent-wave-induced frequency shift for optical superresolution imaging," *Opt. Lett.* **38**(14), 2455–2458 (2013).
101. R. Ye, Y. H. Ye, H. F. Ma, J. Ma, B. Wang, J. Yao, S. Liu, L. Cao, H. Xu, and J. Y. Zhang, "Experimental far-field imaging properties of a ~5- μm diameter spherical lens," *Opt. Lett.* **38**(11), 1829–1831 (2013).
102. S. Lee, L. Li, Z. Wang, W. Guo, Y. Yan, and T. Wang, "Immersed transparent microsphere magnifying sub-diffraction-limited objects," *Appl. Opt.* **52**(30), 7265–7270 (2013).
103. C. Pérez-Rodríguez, S. Ríos, I. R. Martín, L. L. Martín, P. Haro-González, and D. Jaque, "Upconversion emission obtained in Yb^{3+} - Er^{3+} doped fluoroindate glasses using silica microspheres as focusing lens," *Opt. Express* **21**(9), 10667–10675 (2013).
104. Y. Duan, G. Barbastathis, and B. Zhang, "Classical imaging theory of a microlens with super-resolution," *Opt. Lett.* **38**(16), 2988–2990 (2013).
105. Y. Yan, L. Li, C. Feng, W. Guo, S. Lee, and M. Hong, "Microsphere-coupled scanning laser confocal nanoscope for sub-diffraction-limited imaging at 25 nm lateral resolution in the visible spectrum," *ACS Nano* **8**(2), 1809–1816 (2014).
106. A. Darafsheh, N. I. Limberopoulos, J. S. Derov, D. E. Walker, Jr., and V. N. Astratov, "Advantages of microsphere-assisted super-resolution imaging technique over solid immersion lens and confocal microscopies," *Appl. Phys. Lett.* **104**(6), 061117 (2014).
107. K. W. Allen, A. Darafsheh, F. Abolmaali, N. Mojaverian, N. I. Limberopoulos, A. Lupu, and V. N. Astratov, "Microsphere-chain waveguides: Focusing and transport properties," *Appl. Phys. Lett.* **105**(2), 021112 (2014).

108. V. M. Sundaram and S.-B. Wen, "Analysis of deep sub-micron resolution in micro-sphere based imaging," *Appl. Phys. Lett.* **105**(20), 204102 (2014).
109. R. Ye, Y. H. Ye, H. F. Ma, L. Cao, J. Ma, F. Wyrowski, R. Shi, and J. Y. Zhang, "Experimental imaging properties of immersion microscale spherical lenses," *Sci. Rep.* **4**(1), 3769 (2015).
110. X. Xie, Y. Chen, K. Yang, and J. Zhou, "Harnessing the point-spread function for high-resolution far-field optical microscopy," *Phys. Rev. Lett.* **113**(26), 263901 (2014).
111. X. Huang, X. N. He, W. Xiong, Y. Gao, L. J. Jiang, L. Liu, Y. S. Zhou, L. Jiang, J. F. Silvain, and Y. F. Lu, "Contrast enhancement using silica microspheres in coherent anti-Stokes Raman spectroscopic imaging," *Opt. Express* **22**(3), 2889–2896 (2014).
112. E. McLeod and A. Ozcan, "Nano-imaging enabled via self-assembly," *Nano Today* **9**(5), 560–573 (2014).
113. S. Peng, C. Xu, T. C. Hughes, and X. Zhang, "From nanodroplets by the ouzo effect to interfacial nanolenses," *Langmuir* **30**(41), 12270–12277 (2014).
114. Y. Yan, Y. Zeng, Y. Wu, Y. Zhao, L. Ji, Y. Jiang, and L. Li, "Ten-fold enhancement of ZnO thin film ultraviolet-luminescence by dielectric microsphere arrays," *Opt. Express* **22**(19), 23552–23564 (2014).
115. P. K. Upputuri, Z. Wu, L. Gong, C. K. Ong, and H. Wang, "Super-resolution coherent anti-Stokes Raman scattering microscopy with photonic nanojets," *Opt. Express* **22**(11), 12890–12899 (2014).
116. V. M. Sundaram and S. B. Wen, "Analysis of deep sub-micron resolution in microsphere based imaging," *Appl. Phys. Lett.* **105**(20), 204102 (2014).
117. Y. V. Miklyaev, S. A. Asselborn, K. A. Zaytsev, and M. Y. Darscht, "Superresolution microscopy in far-field by near-field optical random mapping nanoscopy," *Appl. Phys. Lett.* **105**(11), 113103 (2014).
118. M. Michihata, K. Takami, T. Hayashi, and Y. Takaya, "Fundamental validation for surface texture imaging using a microsphere as a laser-trapping-based microprobe," *Adv. Opt. Technol.* **3**, 417–423 (2014).
119. S. Mandal, "Superlens-Based Nanoscale Imaging," *IEEE Potentials* **33**(2), 17–20 (2014).
120. A. Darafsheh, C. Guardiola, A. Palovcak, J. C. Finlay, and A. Cárabe, "Optical super-resolution imaging by high-index microspheres embedded in elastomers," *Opt. Lett.* **40**(1), 5–8 (2015).
121. M. Guo, Y.-H. Ye, J. Hou, and B. Du, "Experimental far-field imaging properties of high refractive index microsphere lens," *Photonics Research* **3**(6), 339–342 (2015).
122. H. Pang, A. Cao, C. Du, Q. Qiu, Q. Deng, and S. Yin, "Spectrum analysis of liquid immersion to transparent microsphere based optical nanoscopy," *Optik (Stuttg.)* **126**(21), 3079–3083 (2015).
123. H. Zhu, B. Yan, S. Zhou, Z. Wang, and L. Wu, "Synthesis and superresolution imaging performance of a refractive-index-controllable microsphere superlens," *J. Mater. Chem. C Mater. Opt. Electron. Devices* **3**(41), 10907–10915 (2015).
124. S. Lee and L. Li, "Rapid super-resolution imaging of sub-surface nanostructures beyond diffraction limit by high refractive index optical nanoscopy," *Opt. Commun.* **334**, 253–257 (2015).
125. K. W. Allen, N. Farahi, Y. Li, N. I. Limberopoulos, D. E. Walker, Jr., A. M. Urbas, and V. N. Astratov, "Overcoming the diffraction limit of imaging nanoplasmonic arrays by microspheres and microfibers," *Opt. Express* **23**(19), 24484–24496 (2015).
126. T. X. Hoang, Y. Duan, X. Chen, and G. Barbastathis, "Focusing and imaging in microsphere-based microscopy," *Opt. Express* **23**(9), 12337–12353 (2015).
127. S. Lee and L. Li, "Rapid super-resolution imaging of sub-surface nanostructures beyond diffraction limit by high refractive index microsphere optical nanoscopy," *Opt. Commun.* **334**, 253–257 (2015).
128. K. W. Allen, N. Farahi, Y. Li, N. I. Limberopoulos, D. E. Walker, Jr., A. M. Urbas, V. Liberman, and V. N. Astratov, "Super-resolution microscopy by movable thin-films with embedded microspheres: Resolution analysis," *Ann. Phys.* **527**(7-8), 513–522 (2015).
129. C. Zheng, A. Hu, K. D. Kihm, Q. Ma, R. Li, T. Chen, and W. W. Duley, "Femtosecond Laser Fabrication of Cavity Microball Lens (CMBL) inside a PMMA Substrate for Super-Wide Angle Imaging," *Small* **11**(25), 3007–3016 (2015).
130. L. Yao, Y. H. Ye, H. F. Ma, L. Cao, and J. Hou, "Role of the immersion medium in the microscale spherical lens imaging," *Opt. Commun.* **335**, 23–27 (2015).
131. H. Cang, A. Salandrino, Y. Wang, and X. Zhang, "Adiabatic far-field sub-diffraction imaging," *Nat. Commun.* **6**, 7942 (2015).
132. L. Cao, Y. H. Ye, L. Yao, and M. Guo, "Dependence of focal position on the microscale spherical lens imaging," *Opt. Commun.* **353**, 184–188 (2015).
133. H. Yang and M. A. M. Gijs, "Optical microscopy using a glass microsphere for metrology of sub-wavelength nanostructures," *Microelectron. Eng.* **143**, 86–90 (2015).
134. J. Hou, L. Yao, J. Ren, M. Guo, and Y.-H. Ye, "Magnification and resolution of microlenses with different shapes," *IET Micro & Nano Letters* **10**(7), 351–354 (2015).
135. Y. Chen, X. Xie, L. Li, G. Chen, L. Guo, and X. Lin, "Improving field enhancement of 2D hollow tapered waveguides via dielectric microcylinder coupling," *J. Phys. D Appl. Phys.* **48**(6), 065103 (2015).
136. Y. Li, Z. Shi, S. Shuai, and L. Wang, "Widefield scanning imaging with optical super-resolution," *J. Mod. Opt.* **62**(14), 1033–1036 (2015).
137. H. Pang, A. Cao, C. Du, Q. Qiu, Q. Deng, and S. Yin, "Spectrum analysis of liquid immersion to transparent microsphere based optical nanoscopy," *Optik (Stuttg.)* **126**(21), 3079–3083 (2015).
138. M. Guo, Y. H. Ye, J. Hou, and B. Du, "Experimental far-field imaging properties of high refractive index microsphere lens," *Photonics Research* **3**(6), 339–342 (2015).

139. B. Yan, L. Yue, and Z. Wang, "Engineering near-field focusing of a microsphere lens with pupil masks," *Opt. Commun.* **370**, 140–144 (2016).
140. Z. Wang, "Microsphere super-resolution imaging," *Nanoscience* **3**, 193–210 (2016).
141. Z. B. Wang, B. Yan, L. Yue, R. K. Leach, and B. Luk'yanchuk, "Solid-Immersion Microsphere Superlens," <http://www.metaconferences.org/ocs/public/conferences/9/pdf/3188.pdf> (2016).
142. W. Fan, B. Yan, Z. Wang, and L. Wu, "Three-dimensional all-dielectric metamaterial solid immersion lens for subwavelength imaging at visible frequencies," *Sci. Adv.* **2**(8), e1600901 (2016).
143. J. N. Monks, B. Yan, N. Hawkins, F. Vollrath, and Z. Wang, "Spider Silk: Mother Nature's Bio-Superlens," *Nano Lett.* **16**(9), 5842–5845 (2016).
144. B. Yan, Z. Wang, A. Parker, Y. Lai, and J. Thomas, "Superlensing Microscope Objective Lens," arXiv:1611.00077 (2016).
145. K. W. Allen, F. Abolmaali, J. M. Duran, G. Ariawansa, N. L. Limberopoulos, A. M. Urbas, and V. N. Astratov, "Increasing sensitivity and angle-of-view of mid-way infrared detectors by integration with dielectric microspheres," *Appl. Phys. Lett.* **108**(24), 241108 (2016).
146. A. V. Maslov and V. N. Astratov, "Imaging of sub-wavelength structures radiating coherently near microspheres," *Appl. Phys. Lett.* **108**(5), 051104 (2016).
147. H. Yang, R. Trouillon, G. Huszka, and M. A. M. Gijs, "Super-resolution imaging of a dielectric microsphere is governed by the waist of its photonic nanojet," *Nano Lett.* **16**(8), 4862–4870 (2016).
148. Y. Ben-Aryeh, "Increase of resolution by use of microspheres related to complex Snell's law," *J. Opt. Soc. Am. A* **33**(12), 2284–2288 (2016).
149. B. Du, Y. H. Ye, J. Hou, M. Guo, and T. Wang, "Sub-wavelength image stitching with removable microsphere-embedded thin film," *Appl. Phys., A Mater. Sci. Process.* **122**(1), 1–6 (2016).
150. F. Wang, L. Liu, P. Yu, Z. Liu, H. Yu, Y. Wang, and W. J. Li, "Three-Dimensional Super-Resolution Morphology by Near-Field Assisted White-Light Interferometry," *Sci. Rep.* **6**(1), 24703 (2016).
151. H. S. S. Lai, F. Wang, Y. Li, B. Jia, L. Liu, and W. J. Li, "Super-Resolution Real Imaging in Microsphere-Assisted Microscopy," *PLoS One* **11**(10), e0165194 (2016).
152. X. Yang, H. Xie, E. Alonas, Y. Liu, X. Chen, P. J. Santangelo, Q. Ren, P. Xi, and D. Jin, "Mirror-enhanced super-resolution microscopy," *Light Sci. Appl.* **5**(6), e16134 (2016).
153. J. Li, W. Liu, T. Li, I. Rozen, J. Zhao, B. Bahari, B. Kante, and J. Wang, "Swimming Microbot Optical Nanoscopy," *Nano Lett.* **16**(10), 6604–6609 (2016).
154. E. Bor, M. Turdnev, and H. Kurt, "Differential evolution algorithm based photonic structure design: numerical and experimental verification of subwavelength $\lambda/5$ focusing of light," *Sci. Rep.* **6**(1), 30871 (2016).
155. P. Y. Li, Y. Tsao, Y. J. Liu, Z. X. Lou, W. L. Lee, S. W. Chu, and C. W. Chang, "Unusual imaging properties of superresolution microspheres," *Opt. Express* **24**(15), 16479–16486 (2016).
156. H. Zhu, W. Fan, S. Zhou, M. Chen, and L. Wu, "Polymer Colloidal Sphere-Based Hybrid Solid Immersion Lens for Optical Super-Resolution Imaging," *ACS Nano* **10**(10), 9755–9761 (2016).
157. G. Gu, R. Zhou, H. Xu, G. Cai, and Z. Cai, "Subsurface nano-imaging with self-assembled spherical cap optical nanoscopy," *Opt. Express* **24**(5), 4937–4948 (2016).
158. M. Wu, R. Chen, J. Soh, Y. Shen, L. Jiao, J. Wu, X. Chen, R. Ji, and M. Hong, "Super-focusing of center-covered engineered microsphere," *Sci. Rep.* **6**(1), 31637 (2016).
159. C. Xu, S. Zhang, J. Shao, B. R. Lu, R. Mehfuz, S. Drakeley, F. Huang, and Y. Chen, "Photon nanojet lens: design, fabrication and characterization," *Nanotechnology* **27**(16), 165302 (2016).
160. M. Guo, Y. H. Ye, J. Hou, B. Du, and T. Wang, "Imaging of sub-surface nanostructures by dielectric planar cavity coupled microsphere lens," *Opt. Commun.* **383**, 153–158 (2017).
161. M. Guo, Y. H. Ye, J. Hou, and B. Du, "Size-dependent optical imaging properties of high-index immersed microsphere lens," *Appl. Phys. B* **122**(3), 1–7 (2016).
162. M. S. Kim, T. Scharf, S. Mühlig, M. Fruhnert, C. Rockstuhl, R. Bitterli, W. Noell, R. Voelkel, and H. P. Herzig, "Refraction limit of miniaturized optical systems: a ball-lens example," *Opt. Express* **24**(7), 6996–7005 (2016).
163. B. Richards and E. Wolf, "Electromagnetic diffraction in optical systems. II. Structure of the image field in an aplanatic system," *Proc. R. Soc. Lond. A Math. Phys. Sci.* **253**(1274), 358–379 (1959).
164. P. R. Selvin and H. Taekjip, *Single-molecule techniques: a laboratory manual* (Cold Spring Harbor Laboratory Press, 2008).
165. A. Vlad, I. Huynen, and S. Melinte, "Wavelength-scale lens microscopy via thermal reshaping of colloidal particles," *Nanotechnology* **23**(28), 285708 (2012).
166. H. Yang, N. Moullan, J. Auwerx, and M. A. M. Gijs, "Super-resolution biological microscopy using virtual imaging by a microsphere nanoscope," *Small* **10**(9), 1712–1718 (2014).
167. L. Li, W. Guo, Y. Yan, S. Lee, and T. Wang, "Label-free super-resolution imaging of adenoviruses by submerged microsphere optical nanoscopy," *Light Sci. Appl.* **2**(9), e104 (2013).
168. F. Wang, L. Liu, H. Yu, Y. Wen, P. Yu, Z. Liu, Y. Wang, and W. J. Li, "Scanning superlens microscopy for non-invasive large field-of-view visible light nanoscale imaging," *Nat. Commun.* **7**, 13748 (2016).
169. B. Yan, Z. Wang, A. I. Parker, Y.-K. Lai, P. J. Thomas, L. Yue and J. N. Monks, "Superlensing microscope objective lens," *Appl. Opt.* **56**, 3142–3144 (2017).
170. V. N. Astratov and A. Darafsheh, "Methods and systems for super-resolution optical imaging using high-index of refraction microspheres and micro-cylinders," US patent application 2014/0355108 A1.

- 171.K. W. Allen, N. Farahi, Y. Li, N. I. Limberopoulos, D. E. Walker, A. M. Urbas, V. Liberman, and V. N. Astratov, "Super-resolution by microspheres and fibers - Myth or reality?" In 17th International Conference on Transparent Optical Networks (ICTON) IEEE, pp. 1–4 (2015).
- 172.S. Kawata and T. Sugiura, "Movement of micrometer-sized particles in the evanescent field of a laser beam," *Opt. Lett.* **17**(11), 772–774 (1992).
- 173.E. E. Narimanov, "The resolution limit for far-field optical imaging," In Lasers and Electro-Optics (CLEO), IEEE, pp. 1–2 (2013).
- 174.J. B. Pendry, "Negative refraction makes a perfect lens," *Phys. Rev. Lett.* **85**(18), 3966–3969 (2000).
- 175.S. A. Claridge, A. W. Castleman, Jr., S. N. Khanna, C. B. Murray, A. Sen, and P. S. Weiss, "Cluster-assembled materials," *ACS Nano* **3**(2), 244–255 (2009).
- 176.R. Rezvani Naraghi, S. Sukhov, J. J. Sáenz, and A. Dogariu, "Near-Field Effects in Mesoscopic Light Transport," *Phys. Rev. Lett.* **115**(20), 203903 (2015).
- 177.H. Zhu, W. Fan, S. Zhou, M. Chen, and L. Wu, "Polymer Colloidal Sphere-Based Hybrid Solid Immersion Lens for Optical Super-Resolution Imaging," *ACS Nano* **10**(10), 9755–9761 (2016).
- 178.H. Zhu, M. Chen, S. Zhou, and L. Wu, "Synthesis of High Refractive Index and Shape Controllable Colloidal Polymer Microspheres for Super-Resolution Imaging," *Macromolecules* **50**(2), 660–665 (2017).
- 179.A. Szameit, Y. Shechtman, E. Osherovich, E. Bullich, P. Sidorenko, H. Dana, S. Steiner, E. B. Kley, S. Gazit, T. Cohen-Hyams, S. Shoham, M. Zibulevsky, I. Yavneh, Y. C. Eldar, O. Cohen, and M. Segev, "Sparsity-based single-shot subwavelength coherent diffractive imaging," *Nat. Mater.* **11**(5), 455–459 (2012).
- 180.A. I. Kuznetsov, A. E. Miroshnichenko, M. L. Brongersma, Y. S. Kivshar, and B. Luk'yanchuk, "Optically resonant dielectric nanostructures," *Science* **354**(6314), aag2472 (2016).

1. Introduction (Photonic nanojet - a discovery that did not happen 400 years ago)

Transparent spherical particles have been attracting the attention of scientist for more than two millennia. For example, it's been known since ancient times that the garden should not be watered in the afternoon, as the small droplets of water deposited on the leaves could cause sunburns. Pliny the Elder (AD 23–AD 79) reported on the incendiary action of glass spheres and Seneca (4 BC–AD 65) wrote about the magnifying effect of such spheres if one looks through it at small letters. Archimedes, Ptolemy and apparently most antique physicists knew the effect of light refraction. However, to establish the correct law of light refraction was not easy. The history of this discovery is connected with the names of some of the greatest scientists of the Reformation. However, historical analysis [1] shows that this law, in its correct form, was firstly discovered by the scientist Ibn Sahl at the court of Baghdad in 984 and later rediscovered several times by Thomas Harriot in 1602, Johannes Kepler in 1604, Willebrord Snellius (Snell) in 1621 and Rene Descartes in 1637. In 1662 Pierre de Fermat showed that this law follows from Fermat's Principle, which establishes that light follows the path that minimizes the time. In 1678 Christiaan Huygens showed how Snell's law of sines could be explained using the wave nature of light and Huygens–Fresnel principle.

In 1604 Kepler introduced the meaning of focus and explained the principles of pinhole cameras. In his book published in 1611 he describes light refraction and the concept of the optical image. He yielded also the general theory of lenses. Kepler was familiar with the law of sines and knew the trigonometric tables of Rheticus, published in 1551, as well as Napier's tables of logarithms. Galileo also was familiar with the "science of refraction", as he wrote in his *Sidereus Nuncius*, 1610. At the same time, later Galileo wrote to Giovanni Tarde in his letter on November of 1614: "This science is still not well known, and I do not know anyone who would be engaged in it, unless the recall of Johannes Kepler, the Imperial mathematician who wrote a book about it, but it is so dark that it is perhaps no one understood". Probably these words explain why the discovery of *photonic nanojets* did not happen 400 years ago, despite Kepler having sufficient skills to explain the effects described by Pliny and Seneca on the basis of ray tracing and geometrical optics. Kepler was also familiar with a question debated by ancient scholastics: "Whether a million of Angels may not fit upon a needle's point?" Can one ask the same question about the pieces of light at the nanoscale?

The story of Snell's law is a particular example of the general Arnold Principle [2]: "If a notion bears a personal name, then this name is not the name of the discoverer".

In any case, it is not difficult to reproduce ray tracing [3] pictures, which Kepler and Snell, in principle, were able to plot, from which one can see effect of light focusing by dielectric spheres and cylinders. For spheres with refractive index $1 < n < 2$, the focus is situated at some distance on the shadow-side surface. For $n = 2$, the focusing happens, exactly, on the shadow-side surface. Finally, for all $n > 2$ the light is focused inside the particle. Following Snell's law one can find [3] both the caustic shape and the cusp end at the geometrical-optics focus, which is situated at a distance $f = \frac{R}{2} \frac{n}{n-1}$ (as measured from the center of the sphere). The spot size at this position can be approximated by caustic, and is given by $w = R \sqrt{\frac{(4-n^2)^3}{27n^4}}$. Finally, the field enhancement at the focal point, calculated under the approximation of geometrical optics is given by

$$\frac{I_{\max}}{I_0} \approx \frac{R^2}{w^2} = \frac{27n^4}{(4-n^2)^3}. \quad (1)$$

In the case of a cylinder, a similar formula for the field enhancement can be found, which reads as

$$\frac{I_{\max}}{I_0} \approx \frac{R}{w} = \sqrt{\frac{27n^4}{(4-n^2)^3}}. \quad (2)$$

One can see from these formulas that a large field enhancement appears near the outer edge of the particle. It depends on the refractive index only while the spot size is proportional to the particle size and can be significantly smaller than it.

An important step forward to the study of light scattering by small particles was taken by Lord Rayleigh. From his considerations [4], it follows that a small dielectric particle with size $R \ll \lambda$ does not act as a small lens but, instead, scatters light as a point electric dipole (and therefore symmetrically in the forward and backward directions). Thus, asymmetrical jet-like fields arise just in some range of R/λ values, which could not be small.

The full description of light scattering by spherical particle was obtained by Mie in 1908, and it is known as Mie theory [5]. If the particle has no dissipation the scattering is characterized by the refractive index n_p as well as the size parameter $q = 2\pi R n_m / \lambda$. Here n_m is refractive index of media. According to Mie theory, the total scattering efficiency Q_{sca} as well as the forward, Q_{FS} , and backward, Q_{BS} , scattering efficiencies are represented by [5]

$$Q_{sca} = \frac{2}{q^2} \sum_{\ell=1}^{\infty} (2\ell+1) \left[|a_{\ell}|^2 + |b_{\ell}|^2 \right], \quad (3)$$

$$Q_{FS} = \frac{1}{q^2} \left| \sum_{\ell=1}^{\infty} (2\ell+1)(a_{\ell} + b_{\ell}) \right|^2, \quad Q_{BS} = \frac{1}{q^2} \left| \sum_{\ell=1}^{\infty} (2\ell+1)(-1)^{\ell} (a_{\ell} - b_{\ell}) \right|^2, \quad (4)$$

where the scattering amplitudes a_{ℓ} (electric) and b_{ℓ} (magnetic) are defined by the formulas

$$a_{\ell} = \frac{F_{\ell}^{(a)}}{F_{\ell}^{(a)} + iG_{\ell}^{(a)}}, \quad b_{\ell} = \frac{F_{\ell}^{(b)}}{F_{\ell}^{(b)} + iG_{\ell}^{(b)}}, \quad (5)$$

and the quantities $F_\ell^{(a,b)}$ and $G_\ell^{(a,b)}$ are expressed in terms of the Bessel and Neumann functions:

$$F_\ell^{(a)} = n\psi'_\ell(q)\psi_\ell(nq) - \psi_\ell(q)\psi'_\ell(nq), \quad G_\ell^{(a)} = n\chi'_\ell(q)\psi_\ell(nq) - \psi'_\ell(nq)\chi_\ell(q),$$

$$F_\ell^{(b)} = n\psi'_\ell(nq)\psi_\ell(q) - \psi_\ell(nq)\psi'_\ell(q), \quad G_\ell^{(b)} = n\chi_\ell(q)\psi'_\ell(nq) - \psi_\ell(nq)\chi'_\ell(q). \quad (6)$$

Here $\psi_\ell(q) = \sqrt{\frac{\pi q}{2}} J_{\ell+\frac{1}{2}}(q)$, $\chi_\ell(q) = \sqrt{\frac{\pi q}{2}} N_{\ell+\frac{1}{2}}(q)$, $\psi'_\ell(q) = d\psi_\ell(q)/dq$, $\chi'_\ell(q) = d\chi_\ell(q)/dq$, the symbol ' denotes differentiation with respect to the argument of the corresponding function.

Inside the particle one can find the amplitudes of the internal fields d_ℓ (electric) and c_ℓ (magnetic) which are defined by the formulas:

$$d_\ell = -\frac{in}{F_\ell^{(a)} + iG_\ell^{(a)}}, \quad c_\ell = \frac{in}{F_\ell^{(b)} + iG_\ell^{(b)}}. \quad (7)$$

Similar formulas can be written in the case of light scattering by an infinite circular cylinder [5]. For example, for the case of TE-polarization ($\mathbf{E} \perp z$) and normal incidence the scattering efficiency \bar{Q}_{sca} and differential forward \bar{Q}_{FS} and backscattering \bar{Q}_{BS} efficiencies are given by (an over line is used to distinguish them from those corresponding to spheres):

$$\bar{Q}_{sca} = \frac{2}{q} \sum_{\ell=-\infty}^{\infty} |\bar{a}_\ell|^2, \quad \bar{Q}_{FS} = \frac{2}{\pi q} |f_0|^2, \quad \bar{Q}_{BS} = \frac{2}{\pi q} |f_\pi|^2, \quad (8)$$

where

$$f_0 = \sum_{\ell=-\infty}^{\infty} (-i)^\ell e^{-i\pi\ell/2} \bar{a}_\ell, \quad f_\pi = \sum_{\ell=-\infty}^{\infty} (-i)^\ell (-1)^\ell e^{-i\pi\ell/2} \bar{a}_\ell, \quad \bar{a}_\ell = \frac{\Re_\ell}{\Re_\ell + i\Im_\ell}, \quad (9)$$

and

$$\Re_\ell = nJ_\ell(nq)J'_\ell(q) - J'_\ell(nq)J_\ell(q), \quad \Im_\ell = nJ_\ell(nq)N'_\ell(q) - J'_\ell(nq)N_\ell(q). \quad (10)$$

The amplitudes of internal fields are represented by

$$\bar{d}_\ell = \frac{2}{\pi q} \frac{i}{\Re_\ell + i\Im_\ell}. \quad (11)$$

In contrast to spherical particles, where the electric, a_ℓ , and magnetic, b_ℓ , amplitudes are described by different formulas (5), for the case of cylinders both, electric and magnetic amplitudes, \bar{a}_ℓ , follow the same formula (9). For TE-polarization, the even index corresponds to magnetic modes (\bar{a}_0 - magnetic dipole, \bar{a}_2 - magnetic quadrupole, \bar{a}_4 - magnetic octupole, etc.) and odd index corresponds to electric modes (\bar{a}_1 - electric dipole, \bar{a}_3 - electric quadrupole, etc.). Similar relations are valid for internal field amplitudes \bar{d}_ℓ . Using Mie theory it is easy to see how the field enhancement transforms from that of a dipole in the limit of Rayleigh scattering to a pronounced, jet-like structure near the outer part of the particle as a function of the index of refraction and particle size. Such kind of jet-like structure for small particles has been known at least since the year 2000 [6]. One can see a number of these jets

in the papers [6–10], e.g. Figure 1 where the jet from the front page of the book [10] is shown.

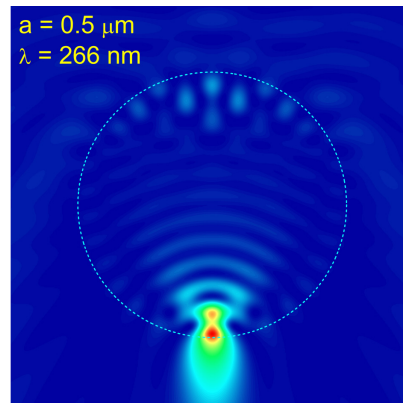


Fig. 1. The image of photonic jet for a particle with $n = 1.6$ from the front page of the book [10]. Original publications related to similar jets one can find in the papers [3, 6–17].

In Fig. 2, we exemplify the mentioned evolution of the field intensity distribution as the size parameter for a spherical particle with refractive index $n = 1.5$ is varied from the Rayleigh limit to the formation of the jet-like structure. At $q = 0.1$ (within the Rayleigh limit) one can see the usual field distribution corresponding to an electric dipole. As the size parameter is increased, the field profile evolves and tends to be more localized into the forward direction. Finally, at $q = 10\pi$ one can see the formation of a pronounced jet (see supplementary video). This effect plays an important role in laser cleaning [6–10] and it can be used for subdiffraction nanopatterning [11–17] of semiconductor, metallic and transparent substrates. Using Mie theory one can study the basic properties of the near field enhancement obtained within the jet-like structures.

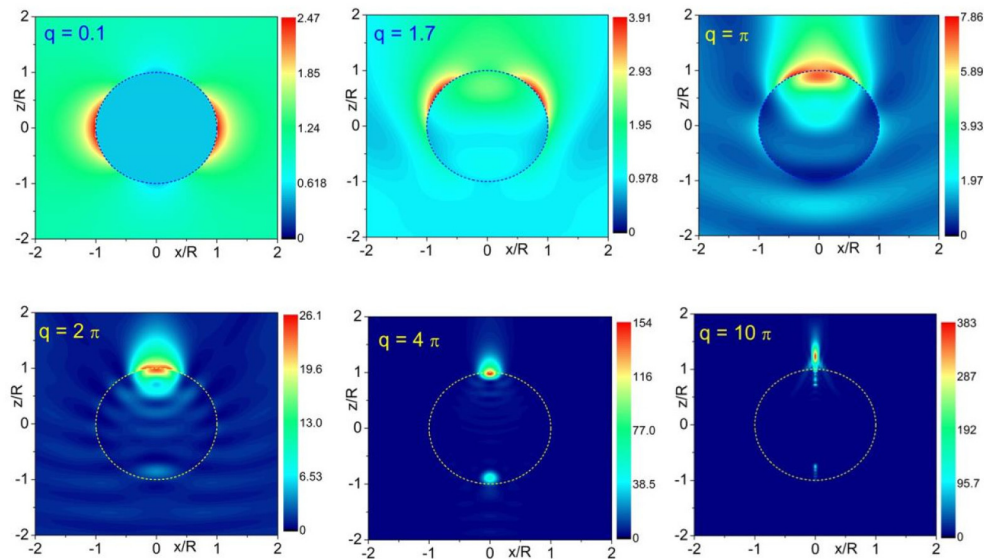


Fig. 2. Intensity \mathbf{E}^2 distribution within the $\{xz\}$ plane through the particle center calculated from the Mie theory for the particle with $n = 1.5$ and different values of the size parameter q .

For large values of the size parameter, the maximum intensity within the jet has an asymptotic dependence $I_{\max} \propto q$ see e.g [3, 17, 18]. This is a typical case for a large particle with large spherical aberration [19] whose geometrical-optics focus scales as $f \propto R$ for spheres. The focal caustic is axially symmetric and highly degenerate [20]. It contains a caustic surface of revolution with $I \propto q^{1/3}$, and a caustic line along the z axis. The former is due to meridional rays, while the latter is due to sagittal rays. A strong spherical aberration significantly decreases the focal intensity, but creates a high intensity line between the sphere and the focus³. In order to reach a two-orders-of-magnitude \mathbf{E}^2 intensity enhancement with spherical particles one needs characteristic size parameters on the order of ten. At the same time, one-order-of-magnitude \mathbf{E}^2 intensity enhancements using cylinders requires size parameters of a few hundred. While the identification of these near field focusing effects was first found in [6–17], the concept was further developed in subsequent works [21–29] in which, additionally, the popular term “*photonic nanojet*” was introduced. Different properties of these jet-like field distributions in particles with different shapes were further investigated in a number of papers, e.g. in [21] the scattering from cylinders with size parameter $q = 10\pi$ and refractive indexes $n = 1.7, 2.5$ and 3.5 was investigated.

2. Basic properties of photonic nanojet

The majority of the studies devoted to photonic nanojet structures has been done for single and chain of spheres [6–17, 22, 24, 26–52] and cylinders [21, 23, 25, 33, 53–59]. In general, the behavior of spheres and cylinders are quite similar and, thus, it makes sense to discuss the results for both shapes in parallel. In Fig. 3 we present the color contour plots of scattering efficiencies for a sphere and a cylinder as a function of their refractive index and size parameter (thus in the $\{q, n\}$ plane), together with the trajectories corresponding to the first three electric and three magnetic resonances. These resonances, for the spherical particle in Fig. 3(a), correspond to the conditions $a_\ell = 1$ and $b_\ell = 1$ while, for the cylindrical particle in Fig. 3(b), they correspond to the conditions $\bar{a}_\ell = 1$. One can see that trajectories of electric dipole (ed) and magnetic quadrupole (mq) for the spherical particle with $1.5 < n < 2$ are quite close. On the contrary, for the cylindrical particle the trajectories of these resonances are clearly separated. On the left hand parts of the contour plots we represent the variation of several individual multipoles as a function of the size parameter, for three particular values of the refractive index: $n = 1.6, 2$ and 2.5 . One can see that resonances become sharper and move towards smaller size parameters with increasing refraction index.

In Fig. 4(a), the total and partial electric and magnetic scattering efficiencies are studied, both, for a sphere and a cylinder. The total scattering efficiency for particles with refractive index $n = 2$, shown in panels (a), can be accurately described in this range of q values as a sum of the six partial resonant efficiencies shown. In the case of sphere, the three observed dominant peaks in Q_{sca} could be identified as corresponding to the dipole, quadrupole and octupole magnetic resonances. In the case of a cylinder, the effect of overlapping of different resonances is more pronounced, and no clear peaks are observed in the total scattering efficiency.

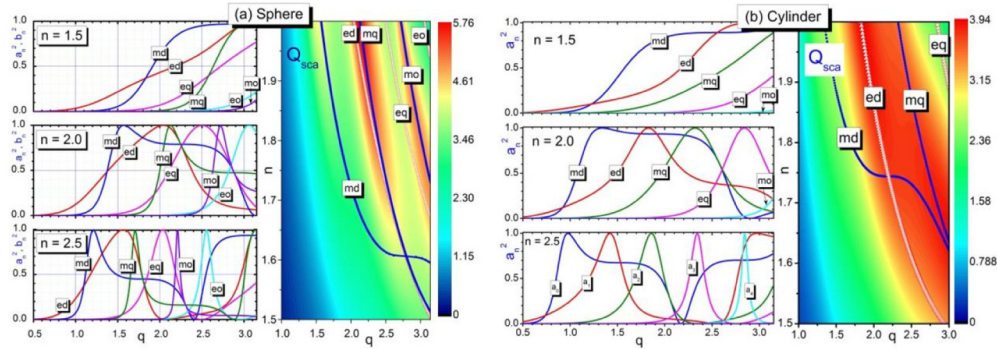


Fig. 3. Left panels (a) show first three electric amplitudes: electric dipole $|a_1|^2$ (ed), electric quadrupole $|a_2|^2$ (eq), electric octupole $|a_3|^2$ (eo) and corresponding first three magnetic amplitudes $|b_1|^2$ (md), $|b_2|^2$ (mq) and $|b_3|^2$ (mo) for a spherical particle as a function of the size parameter for three different values of the index of refraction (indicated in the inset). The color panel on the right shows the contour plot of scattering efficiency Q_{sca} on the $\{q, n\}$ parameters plane, with the trajectories corresponding to the excitation of the different resonances indicated. The panel (b) shows the same as (a) but for a cylindrical particle under TE-polarized light illumination.

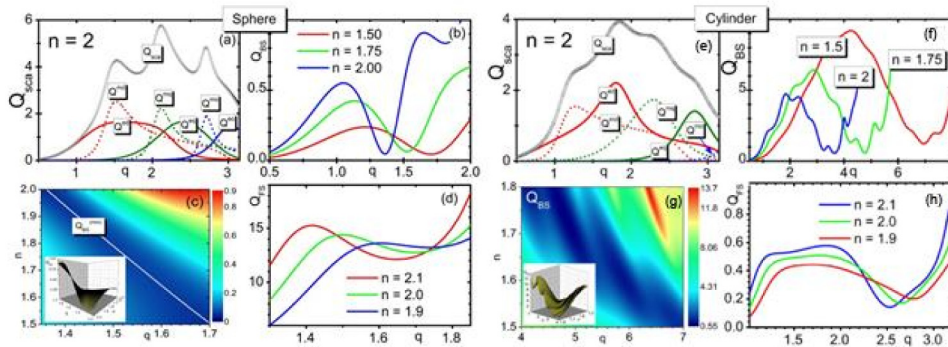


Fig. 4. (a, e) Total scattering efficiency, Q_{sca} , vs size parameter for refractive index $n = 2$ sphere and cylinder. Six partial scattering efficiencies, corresponding to the electric dipole (ed), magnetic dipole (md), electric quadrupole (eq), magnetic quadrupole (mq), electric octupole (eo) and magnetic octupole (mo) contributions. (b, f) Backscattering efficiency Q_{BS} vs size parameter for three different values of refractive index n exhibiting pronounced minima at particular values of size parameter. (c, g) The trajectory of the first Kerker condition [60–62] corresponding to $a_1 = b_1$ on the plane of parameters (n, q) . For a spherical particle it corresponds to a single “canyon” on the $Q_{BS}(n, q)$ surface, see inset. For a cylindrical particle these minima are presented by multiple canyon surfaces. Along these trajectories on the bottom of canyons the polar scattering diagram shows preferentially forward scattering. (d, h) Forward scattering efficiency Q_{FS} vs size parameter for three different values of refractive index n . Interference of electric dipole and magnetic dipole produces the asymmetrical shape in forward scattering.

Overlapping of electric and magnetic resonances yields the first Kerker condition for sphere and cylinder [60, 61], which corresponds to minimal backscattering efficiency. These pronounced minima in backscattering are well seen for, both, sphere and cylinder in Fig. 4(b).

In Fig. 4(c) we show the trajectory of this Kerker resonance for a sphere on the plane of (q, n) parameters. It follows the single valley on the surface and it presents, almost, a linear dependence within the given range of parameters. The polar scattering diagram along Kerker resonance trajectory show pronounced forward scattering (not shown here). The optimum Kerker condition, however, may require a particle with refractive index more than two [62,63]. For example, for a refractive index $n \approx 2.45$, the spheroidal shape can be more efficient [62] than the spherical one. The asymmetrical shape in Fig. 4(d), 4(h) looks like Fano-resonance [64] but it is caused by another type of interference.

In Fig. 5, we show an example of the intensity distribution along the line through the center of a particle with refractive index $n = 1.5$ and size parameter $q = 20$. One can observe a huge field enhancement near the outer edge of the particle. Qualitatively this effect can be understood with the help of ray tracing [3] by Snell's law (shown in the inset). Under the limit of geometrical optics the field enhancement does not depend on the size parameter. In contrast, the wave theory yields strong dependence of the field enhancement on the size parameter.

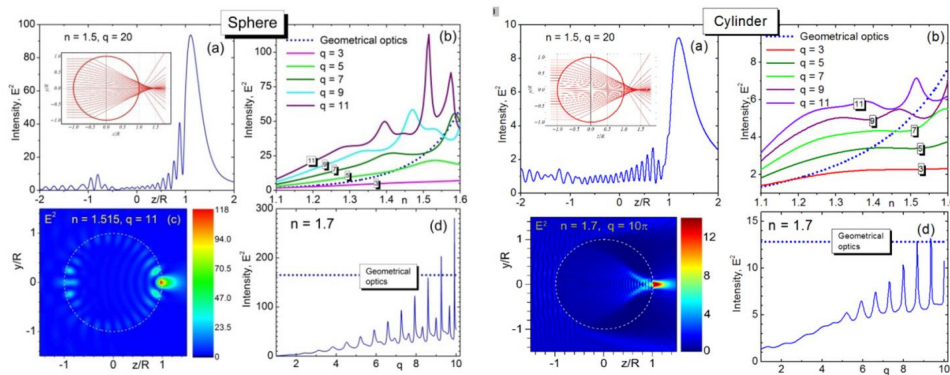


Fig. 5. (a) Intensity distribution along the line through the center of a particle. The particle has a refractive index $n = 1.5$ and size parameter $q = 20$, corresponding to Fig. 4.32 in Ref. [65]. The inset shows the formation of a caustic under the approximation of geometrical optics. (b) Field enhancement vs refractive index for different size parameters. (c) Field distribution in the $\{z, y\}$ cross section of the particle with $n = 1.515$ and $q = 11$. One can see the formation of a whispering gallery mode for the spherical particle. (d) Field enhancement vs size parameter for particle with refractive index $n = 1.7$.

Oscillations in the jet fields caused by optical resonances were discussed since 2000 [6].

In Fig. 6(a) we show these oscillations in the electric field intensity E^2 on the outer edge of the particle on the n and q parameter space. One can clearly see that optical resonances are excited for smaller size parameter with increasing refractive index. Figure 6(b) illustrates the mechanism of field compression by the emergence of optical vortices at the particle border. A zoomed view of these vortices is shown in Fig. 6(c). Singular points marked as 5, 6, 9, 10, 12, 15 are saddles. There are four branches of separatrices emerging from each singular saddle point. Singular points marked as 2, 4, 7, 8, 11, 13, 14 are focal points. The phase trajectories around these points fill the whole space in the corresponding loops.

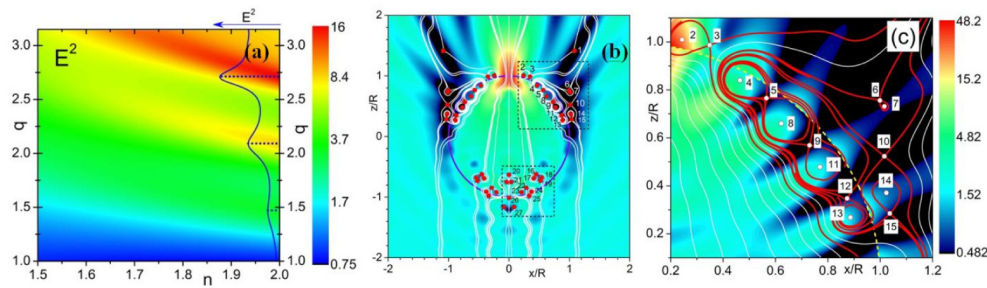


Fig. 6. (a) Color panel representing (in logarithmic scale) the intensity E^2 under a spherical particle on the plane of $\{n, q\}$ parameters. The distribution of intensity vs size parameter for a particle with refractive index $n = 2$ is shown along the right axes of the picture. It clearly shows the excitation of three resonances $q = 1.47, 2.09$ and 2.71 . The latest resonance yields intensity $E^2 \approx 16$. (b) The Poynting vector field distribution for a particle with $n = 1.5$ and size parameter $q = 10$. The colour contour plot represents the modulus $|S|$ in logarithmic scale. There are a number of singular points (52 in total) where $|S| = 0$. An enlarged picture (zoomed) of the Poynting vector field is shown in plot (c) which represents the field lines and singularities of the Poynting vector distribution in the region containing the singular points marked as 2-15. These optical vortices are important in the process of formation of the whispering gallery mode.

There are a few important parameters for the different applications of photonic nanojets. These are, e.g., the position of the focus, the focal spot size, the maximum intensity of the electric and magnetic fields and their dependence on the refractive index and size parameter of the particle. We will now summarize these characteristics for the case of spherical particles. As one can see under the approximation of geometrical optics, the position of the focal point at $n \rightarrow 1$ (n being the relative refractive index between the particle and the external medium) tends to infinity. At $n \rightarrow 2$ the focal point moves towards the particle edge $f \rightarrow R$. This tunable-focus effect can be used, e.g., in laser-assisted micro/nano-fabrication [38,46]. Variations of the relative refractive index $n = n_p/n_m$ are easy to perform for any refractive index of the particle, n_p , just varying the refractive index of the external medium, n_m . An example of such tuning, when the external medium surrounding the particle is changed from air to water, is exemplified in Fig. 7. Practically, it can also be done with the help of additional transparent layers of material deposited on the top of surface meant to be processed [38,46]. Additionally, the position of the focus can be controlled with the size parameter, a situation that is exemplified in Fig. 8 for different values of the refractive index and that has been studied in details in [50].

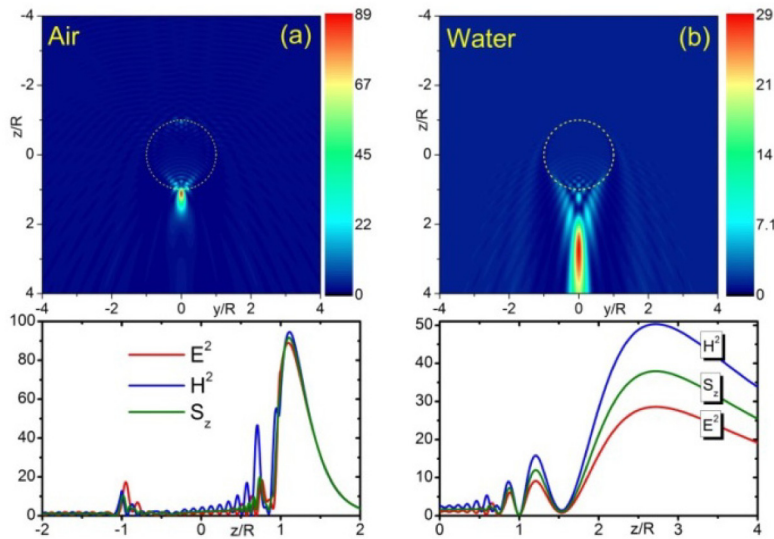


Fig. 7. Cross-sectional view of the normalized local field distribution $|E|^2$ underneath a single particle with $2R = 5 \mu\text{m}$ immersed in (a) air and (b) water [38]. The incident laser beam has a wavelength $\lambda = 800 \text{ nm}$, is linearly polarized along x -axis and propagates along z -axis. The sphere is assumed to be made of quartz $n_p = 1.45332$ and an index $n_m = 1.326$ is assumed for water. The lower panel shows the corresponding distributions along the cut-line passing through the center of the sphere, together with the magnetic field intensity and the z -component S_z of the Poynting vector.

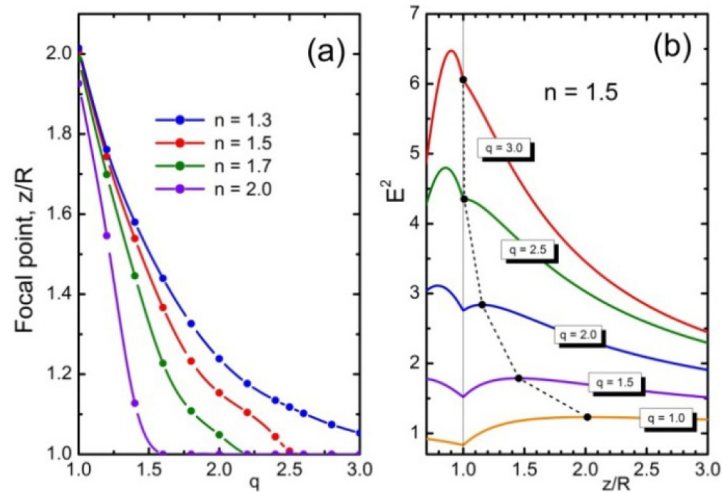


Fig. 8. (a) Position of focal point vs size parameter for different values of refractive index. (b) Distribution of intensity vs z -coordinate (as measured from the center of the particle) for a particle with refractive index $n = 1.5$ and different size parameters. The dashed curve follows the intensity maxima (indicated by solid black points).

As mentioned before, in Mie theory the refractive index enters in the form of the relative refractive index of the particle n_p and the external medium n_m . Thus, it is the ratio n_p/n_m and effective R/λ (R - particle radius, λ - incident wavelength) which are important for

field enhancement. For example, a particle made of TiO_2 ($n_p = 2.5$ in optical range) immersed in water, $n_m = 1.33$, $R/\lambda = 10$, in Fig. 9, have the same properties as a particle with $n_p = 1.88$ embedded in air, with $R/\lambda = 13.3$ (to have the same size parameter). This approach is important for some applications,

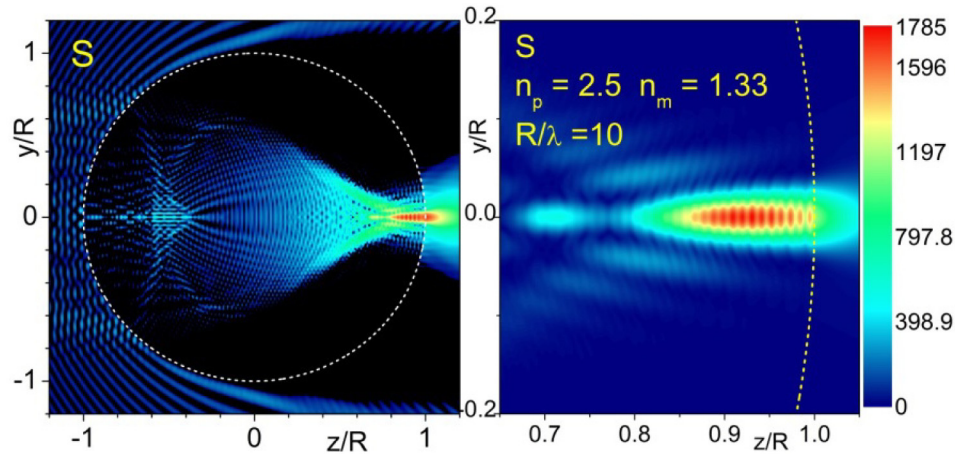


Fig. 9. Field distribution of the Poynting vector for a TiO_2 particle immersed in water. The right panel represents a zoomed view of the intensity distribution near the focal point.

Up to now when referring to the formation of a nanojet, we were describing a phenomenon related to the concentration of electric field. However, for dielectric particles with big size parameters it is interesting to note that the nanojet is, in fact, more a “magnetic nanojet” rather than an “electric nanojet”. This is, when the nanojet is formed, the magnetic field enhancement can be actually much larger than the one corresponding to the electric field. As an example, in Fig. 10 the distribution of electric intensity \mathbf{E}^2 is shown together with magnetic intensity \mathbf{H}^2 and the modulus of the Poynting vector $|\mathbf{S}|$, for a sphere with $n = 1.5$ and size parameter $q = 10$. Therefore, the emergence of enhancements in the magnetic field, identified for particles with high refractive index [66, 67], is also possible for particles with relatively small refractive index $n < 2$, provided their size is larger than the wavelength ($2R \approx 3\lambda$ in this case). This property could be used, for example, to enhance the emission characterized by a magnetic dipole transition [68].

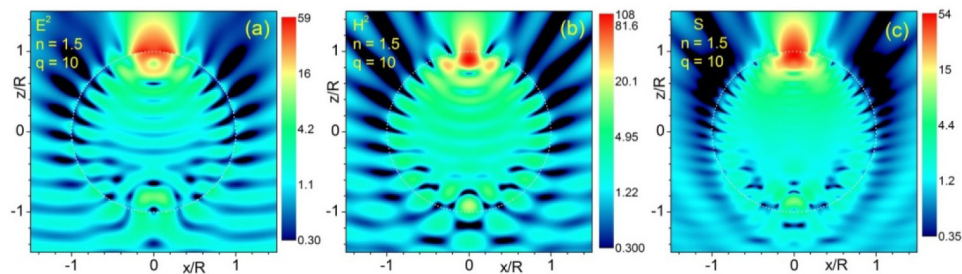


Fig. 10. Distributions of intensity in the $\{x-z\}$ plane of (a) the electric field \mathbf{E}^2 and (b) the magnetic field \mathbf{H}^2 and (c) the modulus of the Poynting vector $|\mathbf{S}|$ for a spherical particle with $n = 1.5$ and size parameter $q = 10$.

3. The caustic structure and shape effects

The majority of applications of nanophotonic jets for nanopatterning were done with particles with size parameters on the order of ten and larger. For these big values of the size parameter Maxwell's equations yield a complex pattern for the electric and magnetic fields, related to caustic diffraction catastrophes [20]. A well-known example of this effect is the generation of Airy patterns [69], which has been discussed due to its relation to super-resolution, near field structure [70]. Another example is the cusp diffraction catastrophe represented by Pearcey function [17, 18, 71]:

$$\Psi(x, z) = \frac{1}{\sqrt{2\pi}} \int_{-\infty}^{\infty} ds \exp \left[i \left(\frac{s^4}{4} + \frac{s^2}{2} z + sx \right) \right] \quad (12)$$

Here Ψ is a complex function of two normalized coordinates, with an intensity defined as $I \propto |\Psi|^2$. The path of integration in (12) is such that the integrand vanishes at its terminal points. The intensity distribution, represented by the Pearcey function [20, 71] is qualitatively similar to those which follow from the solution of the wave equation for the cylinder [72]. The peculiarity of the diffraction pattern for the spherical particle is an additional caustic line along the z-axis [3]. This caustic is responsible for the maximal field intensity under the particle. For very big size parameters the intensity pattern follows the approximation of geometrical optics, with a wave pattern that is universal for the underlying ray structure [18]. The corresponding canonical integral is the Bessoid integral, which is a three-dimensional generalization of the Pearcey integral that approximates the field near an arbitrary two-dimensional cusp. With size parameters $q > 30$ this model produces a pattern which is very close to the pattern obtained by Mie theory (see, e.g., Figs. 7 and 8 of Ref. 18). The high intensity region is narrower than that of an ideal lens of the same aperture at the expense of a smaller longitudinal localization and has a polarization dependent fine structure.

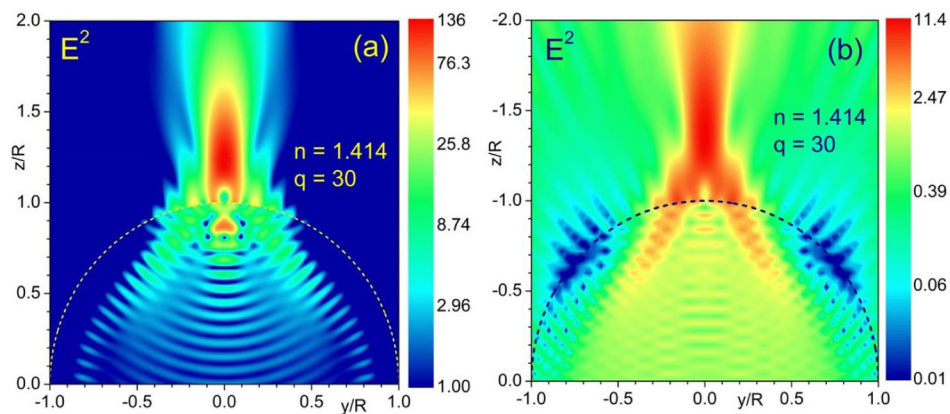


Fig. 11. Electric field intensity patterns for a sphere (a) and cylinder (b) from the same material with refractive index $n = \sqrt{2}$ and size parameter $q = 30$, as seen in [17].

The field enhancement generated from a spherical particle near a surface (particle on surface – theory [6, 73, 74]) can be larger than that obtained in a homogeneous environment (Mie theory). Also, a spherical particle can produce larger intensities than solid immersion lenses (SIL). Some examples of this phenomenon are illustrated in Fig. 11.

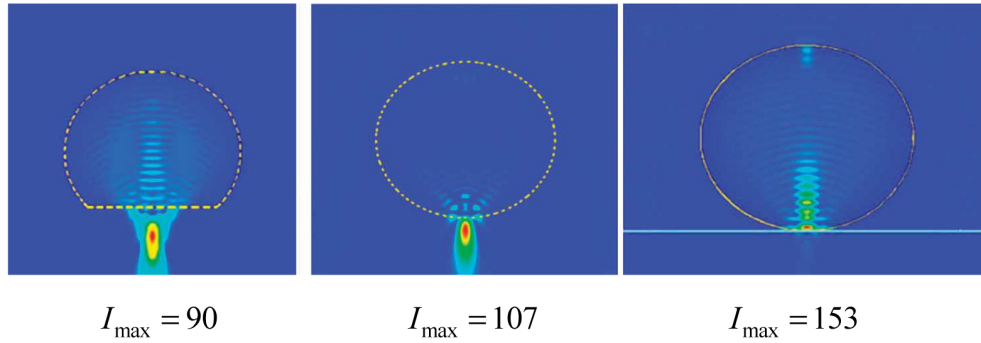


Fig. 12. Electric field intensity distributions calculated for (left panel) a Solid Immersion Lens (SIL): height $h = R(1+1/n) < 2R$, (central panel) a sphere in a homogeneous environment and (right panel) a particle on top of a 40-nm-thick gold film [75]. In all cases the sphere has a radius $R = 2.37 \mu\text{m}$ and a refractive index $n = 1.46$. The operating wavelength is $\lambda = 600 \text{ nm}$.

A number of micro particles with high degree of spatial axial symmetry of the shape (spheres [3, 6–18, 22, 24, 26–52], spheroids [31, 62], cylinders [21, 53, 56, 5, 9], disks [76]) were analyzed in connection to the formation of photonic nanojets. In this regard, the solid immersed lens presented in Fig. 12(a) represents just a particular example. In fact, even particles with non-symmetrical 3D shapes have been shown to produce such photonic jet [77–86]. Some examples of the shapes extensively studied in the literature are presented in Fig. 13.

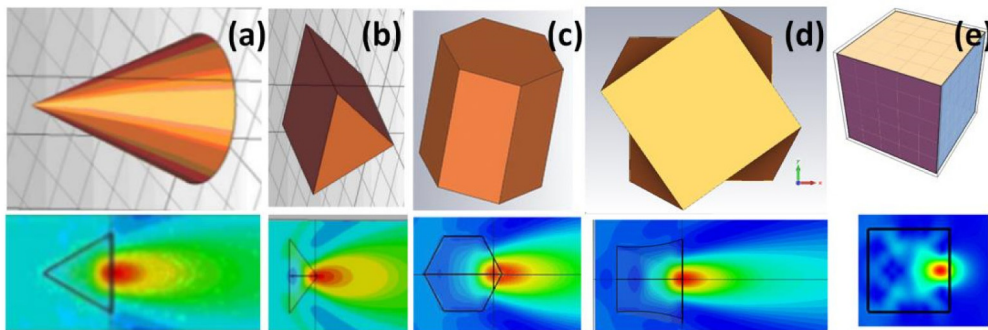


Fig. 13. Dielectric structures of different shapes (top) and intensity distribution of the corresponding photonic nanojets (bottom). (a) A conical structure with $n = 1.6$, height $= \lambda$ and radius of axicon base $= 0.5 \lambda$. (b) A trihedral prism with $n = 1.6$, height $= 0.5\lambda$ and basis $= \lambda$. (c) A hexagonal prism with $n = 1.6$. (d) A deformed cube with chirality, $n = 1.6$. (e) A cube, $n = 1.6$. Adapted from the papers [78, 79, 84, 85].

An interesting modification in the photonic nanojet is present in those structures for which the jet is formed in «reflection» mode; this is, in the case in which the dielectric structure is laying on a highly reflective surface. Such structures were studied, for example, in the cases of spherical [17], hemispherical [83] and rectangular parallelepiped [86] shapes. In Fig. 14(a) the distribution of the z-component of the Poynting vector is represented within the $\{xz\}$ plane. It shows enhanced radiation intensity on top of the particle after the light travels through it upon reflection on the surface. This effect may be find application, for example, in surface enhanced Raman scattering [17]. In Fig. 14(b) and 14(c) a similar reflected jet is represented for the case of a parallelepiped structure [86].

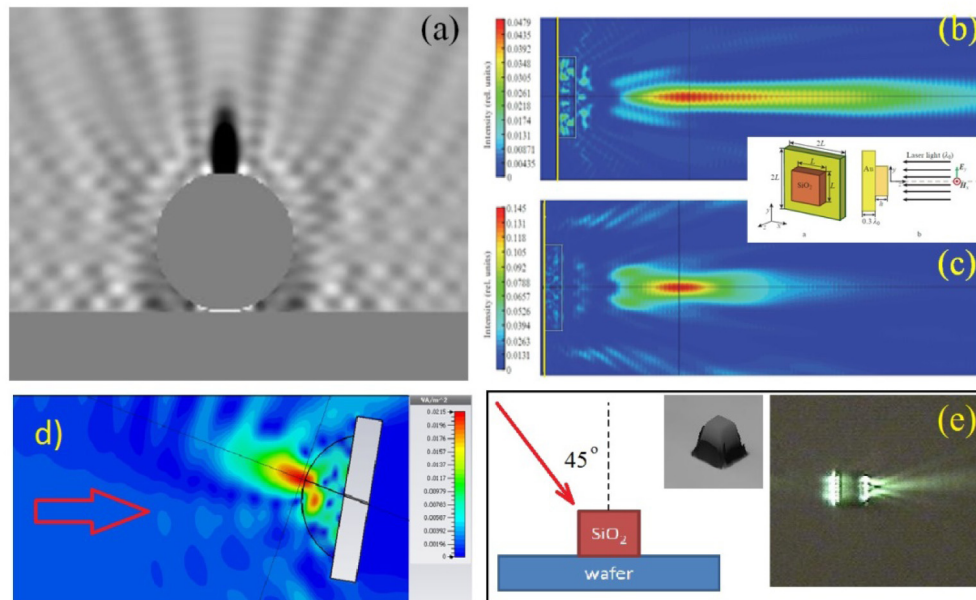


Fig. 14. (a) The intensity $I = S_z$ distribution within the x - z plane for radiation with $\lambda = 248$ nm, scattered by a polystyrene particle ($n = 1.6$, $R = 0.5 \mu\text{m}$) on a silicon surface (calculated using the full analytical solution [17]). The color scale of the intensity varies from negative (*dark*) to positive (*light*) values. The *dark area* on top of the particle corresponds to energy flux directed upwards, while the *white area* under the particle corresponds to the energy flux directed towards the substrate. (b) Photonic jet formed upon reflection of a plane (unfocused) wave from a flat screen with a square dielectric plate embedded in air (the photonic jet length in this example at the level of half the power is 15λ of the incident light). (c) Same as in (b) but when the dielectric plate is embedded in water. The inset shows the corresponding SiO_2 parallelepiped ($n = 1.46$) placed on the metal (gold) substrate. The thickness of the dielectric is $h = 1 \text{ mm}$ and the side of the square is $L = 3.17 \text{ mm}$, the incident radiation has a wavelength of $\lambda = 671 \text{ nm}$. Taken from [86]. (d) and (e) Angular reflected photonic jets. The incident wavelength is 532 nm and the supporting material is a silicon wafer. The focal spot of the laser beam is about 1 mm and the parallelepiped is made of SiO_2 with lateral dimensions of $5 \times 5 \mu\text{m}^2$ and height $1 \mu\text{m}$ (e).

There are a number of modifications of photonic structures which allows the control of the nanojet parameters. For example, to engineer the focusing properties one can use an additional pupil mask or microspheres, decorated with concentric rings [87–89]. This permits an additional reduction of the nanojet focusing spot size.

Another way to improve the nanojet characteristics is using “metamaterial concepts”. In this way one can produce nanojet formation by using a “metalens”, this is, a system composed by a special arrangement some building blocks (“meta-atoms”) or focusing elements. For example, metalenses generated by an assembly of hexagonally arranged, close-contact nanofibers [90] allows creating a nanojet waist smaller than the Abbe diffraction limit.

4. Nanoscopy with microscopic dielectric particles

Photonic jets work, in many ways, similar to optical antennas in the sense that they effectively couple the energy of free-space radiation at optical frequencies to a confined region of subwavelength size. By just time reversal considerations, it is easy to realize that the reversal process should be also possible. In principle, such antenna should also work for near fields in a similar way as SNOM [91] to break the diffraction limit.

In 2009 it was demonstrated that solid immersed lenses (SIL) with $n = 1.5$ can resolve 220 nm structures [92] which was slightly below the diffraction limit for the light used to illuminate the structures, having a wavelength $\lambda = 472$ nm. Later, in Ref [75], it was shown that spherical micrometer-sized particles allow resolving particles strongly below diffraction limit. In this case, the magnified picture of the object, situated close to the particle surface, is related to the virtual image, as shown in Fig. 15. The virtual image magnification factor M for $n < 2$ in the geometrical optics approximation can be calculated through ray tracing for an object in contact with the lens surface [75] (as shown in Figs. 15(a) and 15(b) for a SIL and a spherical particle, respectively) and reads:

$$M_{SIL} = n^2 \quad M_{sphere} = n/(2-n) \quad (13)$$

As one can see in Fig. 15(c) the virtual image generated with a sphere produces a higher magnification than that generated by a SIL. When compared to full electromagnetic analysis, the ray tracing technique gives a qualitatively correct tendency of magnification increase with increasing refractive index, although the geometrical optics approximation fails to predict accurate results near $n = 2$, where the calculated magnification factor tends to infinity. The geometrical optics approximation is also not applicable in near field region, where evanescent fields are present and the problem of microscope resolution beyond the diffraction limit becomes, thus, quite complicated. In any case it was demonstrated in a number of publications [75,92–162] that it is possible to resolve objects below diffraction limit. Experiments were done, both, under white light illumination and with a number of laser wavelengths within the visible range, for particles sizes spanning from submicrometer to hundreds of micrometers and for refractive indexes ranging from 1.3 to 2.5. All papers confirm the magnification effect first described by Seneca. From these publications one can see that, in the case of relatively small magnifications $M = 1.5 - 3$, as those reported e.g. in [95, 109, 120, 121, 123, 124, 126, 130, 134, 142], the solid immersion lens and the spherical particle produce very similar effects. On the contrary, in the range of magnification values $M = 3 - 6$ the difference between a sphere and a SIL becomes pronounced, as reported e.g. in [75, 94, 96, 115, 117, 122, 138, 149, 155, 161]. This latter range of magnifications has been, probably, the most investigated in publications. Finally, there are a few papers in which the authors have used particles with high refractive index $n > 1.8$ and high magnification values $M > 6$ have been obtained. This is the case, e.g., of [95, 116, 147, 151, 153].

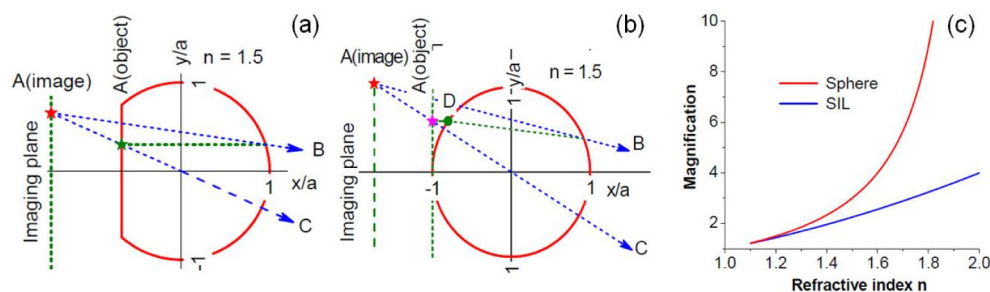


Fig. 15. (a) Ray tracing of virtual image formation in a solid immersion lens (SIL) with thickness $h = R(1 + 1/n)$. (b) Ray tracing of virtual image formation in a spherical particle. (c) Magnification of virtual image versus refractive index in SIL and spherical particle [75].

An example of a microsphere super-resolution imaging [75] setup is illustrated in Fig. 16a. The as-received SiO_2 microspheres were placed on top of nanoscale objects. A halogen lamp with a peak wavelength of 600 nm was used as the white-light illumination source. These microspheres function as super lenses - microsphere super lenses - that collect the underlying near-field object information and magnify it (forming virtual images that keep the

same orientation as the objects in the far-field) before it is projected to an 80X Olympus (Essex, England) objective lens (NA = 0.9, model MDPlan) of an Olympus microscope (model MX-850). The combination of microsphere superlenses and the objective lens forms a compound-imaging lens system. In the reflection mode, the white-light source would be incident from the top, opposite to the light source at the bottom in the transmission mode. Clear images of sub-diffraction-limited features of nanoscale objects have been captured by the nanoscope, as shown in Figs. 15(a)-15(d). For example, 30-nm-thick chrome-film diffraction gratings with 360-nm-wide lines spaced 130 nm apart on fused silica substrates were imaged in transmission mode (see Figs. 16(a) and 16(b)). The virtual image plane was 2.5 μm beneath the substrate surface, and only those lines with microsphere particles on top of them were resolved. The lines without the particles mix together and form a bright spot that cannot be directly resolved by the optical microscope because of the diffraction limit. For the visible wavelength 400 nm, the best diffraction-limited resolution is estimated to be 215 nm in air using the vector theory of Richards and Wolf [163], and 152 nm when taking the solid-immersion effect of a particle into account. For the main peak of a white-light source at 600 nm, such as the ones used in this experiment, the limits are 333 nm in air and 228 nm with solid-immersion effect, respectively. Here, one should also note that the focal planes for the lines with and without particles on top are different. In another example (shown in Figs. 16(c) and 16(d)), a fishnet structure fabricated in a 20-nm thick gold-coated anodic aluminium oxide (AAO) membrane was imaged. The membrane pores are 50 nm in diameter and spaced 50 nm apart. The microsphere nanoscope resolves these tiny pores well beyond the diffraction limit with a resolution between $\lambda/8$ ($\lambda = 400$ nm) and $\lambda/14$ ($\lambda = 750$ nm) in the visible spectral range. It is important to note that the magnification in this case is around 8 X—almost two times that of the earlier grating example, implying that the performance of the microsphere superlens is affected by the near-field interaction of the sphere and the substrate.

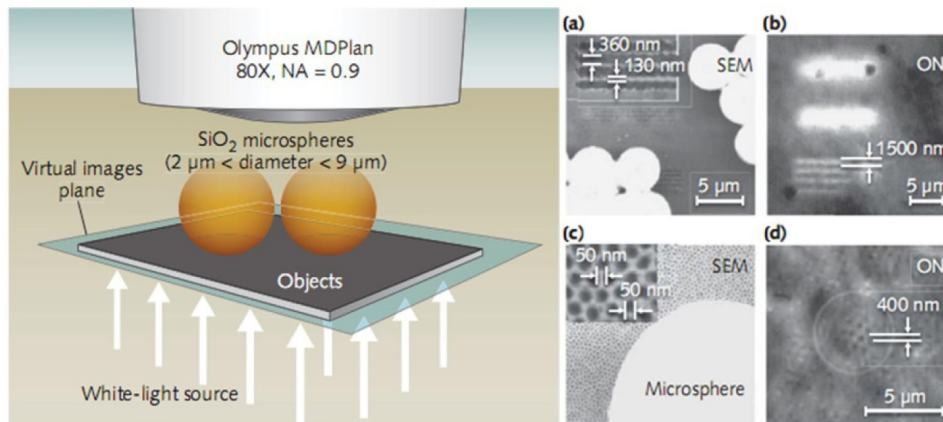


Fig. 16. Schematic showing a white-light microsphere nanoscope (a microsphere superlens integrated with a classical widefield optical microscope) with $\lambda/8$ imaging resolution. The spheres collect the near-field information of the object and form virtual images that are then captured by the conventional lens. (a) to (c) show two examples of microsphere superlenses imaging in transmission mode. In (a)-(b) the object is a diffraction grating with 360-nm-wide lines spaced 130 nm apart. (a) shows an image taken by scanning electron microscope (SEM), while (b) shows the optical nanoscope (ON) image in which the lines are clearly resolved. The magnified image corresponds to a 4.17 X magnification factor. In (c)-(d) the object is gold-coated fishnet membrane sample imaged with a microsphere (size 4.7 μm); (c) shows an SEM image of the object and the microsphere while (d) shows the ON image. The size of the optical image between the pores within the image plane is 400 nm and corresponds to a magnification factor of approximately 8X. The borders of the sphere are shown by white lines. The ON image clearly resolves the pores that are 50 nm in diameter and spaced 50 nm apart.

The field of microsphere nanoscopy has grown rapidly in the past few years. For example, Hao and Liu et al. demonstrated that the imaging contrast in a widefield microsphere nanoscope could be improved by partial immersion of the microspheres in liquid [93]. They also proposed and demonstrated a nice variant of the technique, employing a microfiber to evanescently illuminate the specimen while simultaneously imaging it at a 75-nm resolution [100]. Imaging contrast in this case was greatly improved owing to the limited illumination depth (typically < 200 nm) of the evanescent waves, achieving sharp and clear images of the nanostructures [100]. This idea may be worth of further exploration for sub-50 nm resolution imaging in the future, for example by extending the evanescence wave illumination approach to microspheres using either prism-style or objective-style TIRM (Total Internal Reflection microscopy) setups [164]. Another important development, of particular importance for biological applications, was the demonstration of super-resolution imaging with microspheres inside aqueous environments, where higher-index microspheres [94, 102] were chosen to match the increase in the background liquid medium. Darafsheh et al. [94] have also demonstrated a series of advantages of microsphere-assisted imaging over confocal and solid immersion lens microscopies, including intrinsic flexibility, better resolution, higher magnification, and longer working distances. They were able to resolve minimal feature sizes on the order of 50-60 nm in nanoplasmonic arrays, consistently with previous works [75]. On the other hand, Vlad et al. [165] studied the imaging performance of thermally reshaped polymer microspheres and addressed the issue of virtual image plane selection. In another work, Yan and associates claimed 25 nm lateral resolutions in the visible spectrum by combining fused silica and polystyrene microspheres with a conventional scanning laser confocal microscope [105].

With respect to applications in biological fields, Yang et al.¹⁶⁶ imaged biological samples and demonstrated that the shape of subcellular structures like centrioles, mitochondria and chromosomes can be clearly resolved through a microsphere nanoscope. Similarly, this imaging method [166] was also used to identify the expression of the specific mitochondrial membrane protein MTCO1 and Li et al. applied the technique to image adenovirus without labelling [167].

Practical applications in microscopy require a precise control over the positioning of the microspheres for scanning operation. Different demonstrations, some of which are shown in Fig. 17, have been reported. Krivitsky et al. [95] used a fine glass micropipette attached to the microsphere to move the particle and perform the scanning. Wang et al.¹⁶⁸ extended the development by using an AFM cantilever to mount the microsphere and subsequently used it for precise scanning, achieving high-efficiency super-resolution imaging over a large area, with efficiency 200 times higher than a conventional AFM [95] (as shown in Figs. 17(a) to 17(d)). Li et al. [153] demonstrated the so called swimming micro robot optical nanoscopy (SMON) by using chemical reaction forces to drive the microsphere lens. Autonomous motion and magnetic guidance of micro robots enable large-area, parallel and non-destructive scanning with subdiffraction resolution [153] (as shown in Fig. 17(e)). Another scanning strategy [128, 169, 170] is to use high-index microspheres (TiO_2 or BaTiO_3) embedded into a transparent host material (such as PMMA and PDMS) and then integrate this system with a conventional objective lens, forming a 'superlensing objective lens' (as shown in Figs. 17(f) to 17(h)). The scanning is realized via motion of the imaged objects, which are fixed on a motion stage.

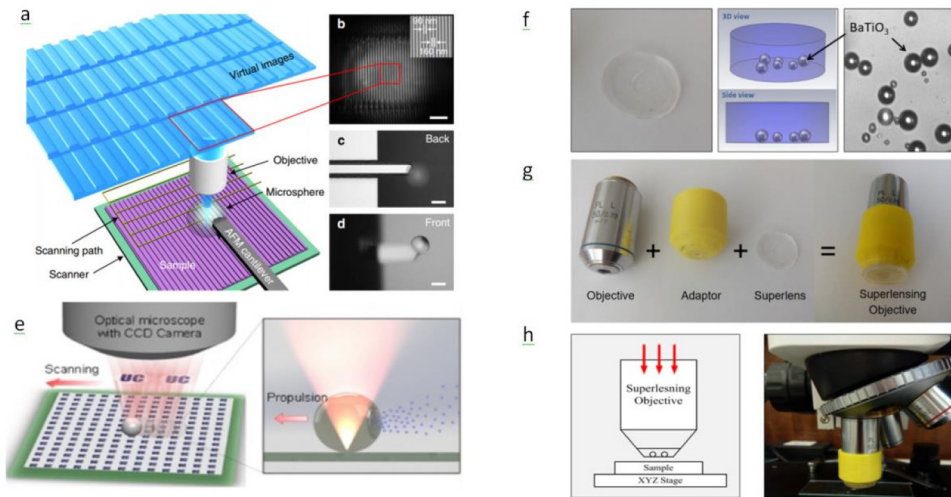


Fig. 17. (a) Scanning superlens attached to a AFM cantilever [168]. (b) Virtual image observed using the microsphere superlens [168]. The inset shows an SEM image of the imaged object [168]. (c, d) Backside and frontside images, respectively, of the AFM cantilever with the attached microsphere superlens. Scale bars correspond to 2 mm in (b) and to 50 mm in (c, d). (e) Swimming micro robot optical nanoscopy [153] (SMON) - schematics and particle scanning mechanism. (f-h) Superlensing objective lenses [169]. In (f) the BaTiO₃ superlens was fabricated by encapsulating a monolayer of BaTiO₃ microspheres (3-80 μm diameter) inside Polydimethylsiloxane (PDMS). In (g) the superlensing objective was made by integrating a conventional microscope objective lens (e.g. 50×, NA = 0.7, or 100×, NA = 0.95) with a BaTiO₃ microsphere superlens using a 3D printed adaptor. (h) Experimental configuration for super-resolution imaging using the developed objective fitted onto a standard white light optical microscope.

Published results of different authors related to magnification M , of virtual images are more or less in agreement with the simplified, geometrical optics approximation in Eqs. (13). However, the reported results on resolution enhancement appear to show large variations between different authors. While the typical resolution of a conventional microscope, $\approx \lambda/2n$, is related to the diffraction limit, when using spherical particle nanoscopes, with refractive indices ranging from relatively low-index $n=1.46$ to relatively high-index $n=1.9-2.1$, different authors have claimed achieved resolutions spanning from $\lambda/3$ to $\lambda/17$ [105]. The resolution variation is caused by the near-field nature of the technique (since the resolution is determined by how much the near-field evanescent waves were collected by the particle in studied particle-on-sample system) as well as the inconsistency in resolution-measurement samples used by different authors (e.g. nano-gaps, nano-lines, nano-grating). For consistency in resolution measurement, one possible solution is to use standard resolution calibration samples such as a nano-scaled version of 1951 USAF resolution test chart which is widely accepted to test the resolution of optical imaging systems such as microscopes, cameras and image scanners. Another solution is to inversely calculate the theoretical point spread function (PSF) from experimental results. In optics, the interconnection between the input pattern $O(x, y)$ in the object space and the output pattern $I(x, y)$ in the image space is described with the help of the $PSF(x, y)$ by the convolution relation

$$I(x, y) = \int_{-\infty}^{\infty} \int_{-\infty}^{\infty} O(u, v) PSF\left(\frac{x}{M} - u, \frac{y}{M} - v\right) du dv, \quad (14)$$

where M is magnification.

If the information about the object is available, this relation can be used to determine the super-resolution experimentally by simple fitting of the measured image [171]. For example, it has been reported that for an imaged object consisting of gold dimers formed by 100 nm disks in diameter separated by a 50 nm gap the convolution calculation yielded a PSF width of $\lambda/7.2$ [171]. This super-resolution effect cannot be explained from the concepts of classical imaging theory [104]: two incoherent dipoles placed on the object plane and just beside a microlens with a diameter of 4.74 μm and a refractive index $n=1.46$ can be resolved using visible light, only, if they are separated by a distance of about 100-150 nm. At the same time, experiments [75] have reported, for the same conditions, a resolution of about 50 nm. In order to correctly estimate the resolution of this system, we cannot simply relate it to the smallest width of the photonic jet associated with the isolated particle. On the contrary, it seems that “particle on surface” effects are necessary to take into account, playing a major role in the correct description of the system. There are a few theoretical models devoted to the formation of virtual images in the near field and the resolution limit in nanoscopy [140]. For example, it was shown [131] that, in the case of two metallic surfaces, the sub-diffraction imaging is possible due to the adiabatic decompression of the plasmon polariton waves excited. Application of this theory to the case of a gold-coated fishnet membrane yields a resolution of about 50 nm. In principle, a similar adiabatic decompression can be realized in the case in which whispering gallery modes are excited instead, as shown in Fig. 18. The imaging process in this case involves two steps. The first step is related to the conversion of the evanescent wave, with wave vector k_e , into a propagating wave, with wave vector k_p , travelling inside the particle. This is a well-known effect described in several works [93, 172]. The second step is the conversion of the wave inside the particle into the far field propagating wave, $k_p \rightarrow k_f$. The characteristic thickness of the evanescent waves scattering zone, d , can be described by [140]:

$$d = R - \sqrt{R^2 - \frac{x^2}{4}} \quad x = \frac{x_p}{M}, \quad (15)$$

where R is the particle radius and x is the size of the sample viewing window which, in turn, can be related to the size of the particle viewing window, x_p , and the magnetization factor, M . This parameter, x , can be computed from the experimental data. For the imaging experiments performed with a 40 nm-thick gold film coated on a glass substrate, in which 40 nm lines separated by 140 nm distance were clearly resolved using a confocal microsphere nanoscope with a 4.7 μm SiO_2 particle ($n=1.46$) [140], the corresponding experimental data of $x_p \approx 3.3 \mu\text{m}$ and $M \approx 3$ yields $x = 1.1 \mu\text{m}$ and $d = 65 \text{ nm}$, which emphasizes the importance of a good near-field contact between particle and sample for the technique. Similar experiments carried out by a different group [105] reported an even better resolution, reaching values of about 25 nm. It is important to note that the quality of the particle and the gold film plays an important role, influencing the decoupling mechanism. Additionally, capillary condensation may influence the structure of the evanescent zone in the gap under the particle. This effect has been reported in a different work [93], in which it was clearly shown that a small layer of liquid on the surface influences the super-resolution capability of the system studied. In fact, even variations in humidity may lead to variations in the nanoscope resolution. This increase in resolution can be simply understood in terms of complex Snell's law [148].

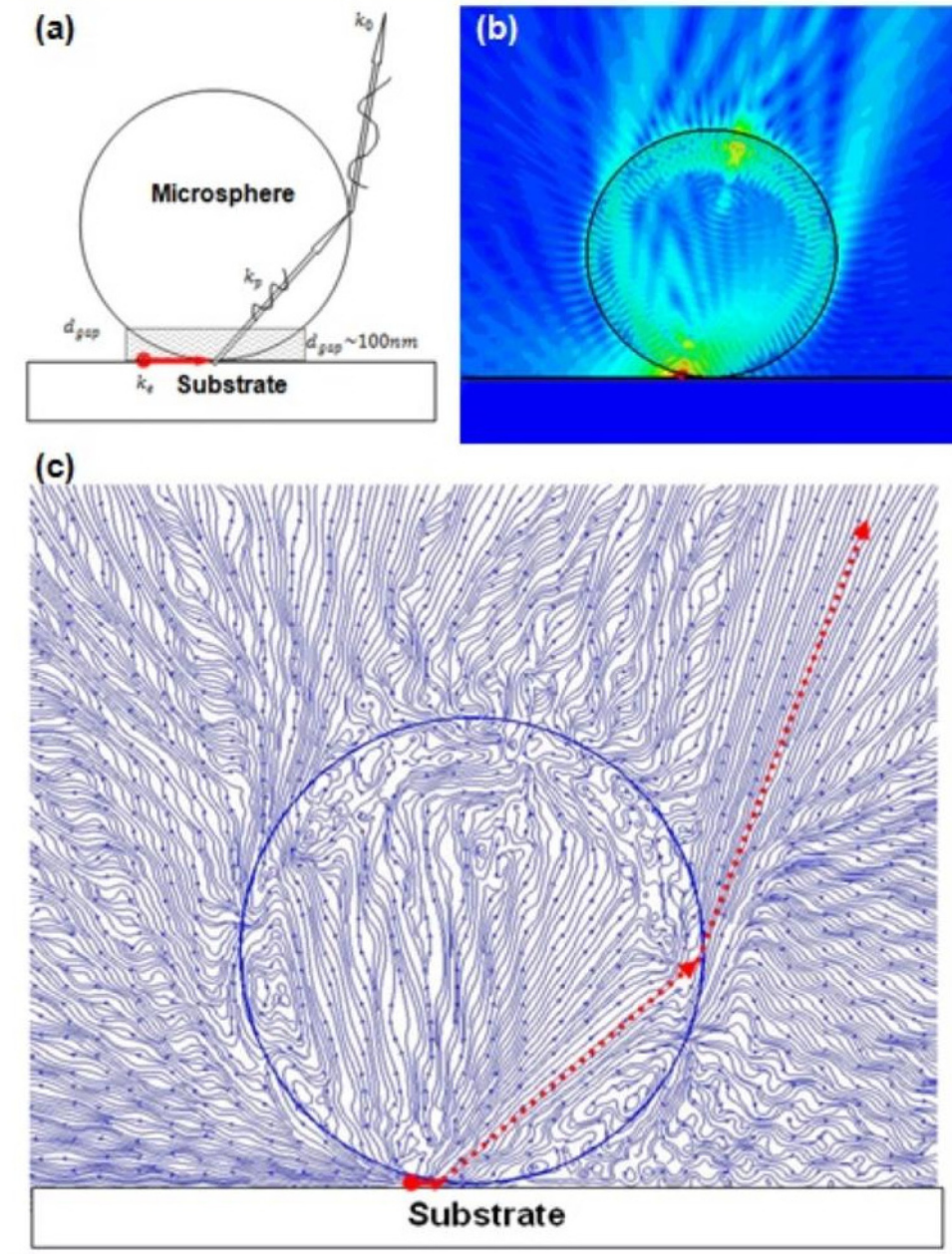


Fig. 18. (a) Schematic description of the decoupling mechanism of high spatial frequency evanescent waves, with wavenumber k_e , by the particle-on-substrate system in a microsphere nanoscope. (b) Calculated distribution of light intensity for a SiO_2 particle on a glass substrate. The particle size is $4.7 \mu\text{m}$ and the incident radiation wavelength $\lambda = 600 \text{ nm}$. (c) Distribution of the Poynting vector in the same situation as (b). A number of vortices can be seen, similar to those shown in Fig. 6, associated to the whispering gallery mode excitation.

In microsphere nanoscope imaging, theoretical analysis of white light interaction with microsphere is often simplified by using its peak wavelength (e.g. 550 nm or 600 nm in most cases), so that the broadband nature of illumination source was neglected. In fact, the

application of white light means the simultaneous excitation of various intensity field patterns across a size parameter range. For example, for a 3- μm -diameter particle under white lights, its size parameter q will range from 13.46 ($\lambda = 700$ nm) to 23.56 ($\lambda = 400$ nm). Using Mie theory we calculated the XZ-plane $|E|^2$ field distribution for varying q with step size accuracy $\Delta q = 0.1$ for both spheres and cylinder, as shown in Fig. 19. For spheres, it shows the co-existence of at least three different field modes or patterns, i.e. super-resolution at $q = 18.4$ (Fig. 19(a)), a usual photonic jet mode (Fig. 19(b)) and a weakly excited whispery gallery mode at $q = 21$ when excited by white light. For cylinder, the results are slight differently, we didn't observe the super-resonance modes in cylinders but see evidence of strongly excited whisper gallery mode at $q = 19.2$ (Fig. 19(e)). It shall be noted these results are calculated with size parameter step size $\Delta q = 0.1$. Reducing Δq step size in calculation may reveal more field patterns due to optical resonances. See [Visualization 1](#) and [Visualization 2](#) with movies for more details on photonic nanojet formation, super resonances in sphere and whispering gallery mode in cylinder.

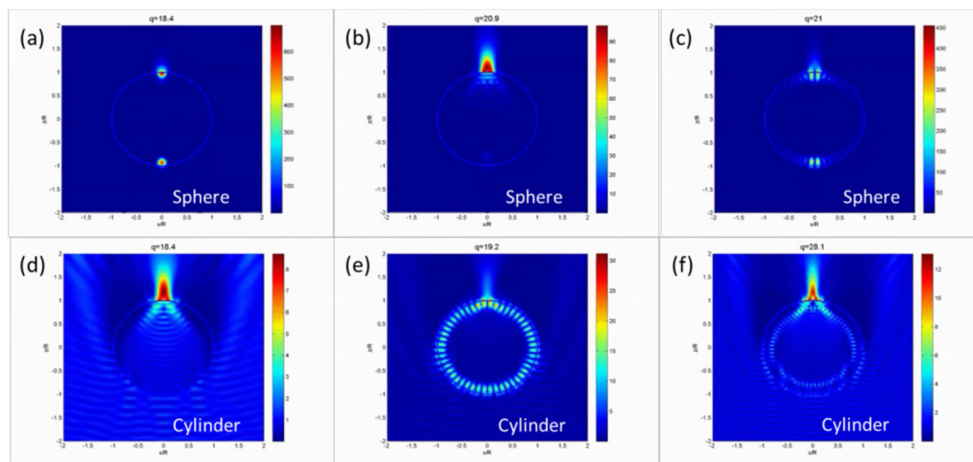


Fig. 19. Typical $|E|^2$ field distributions of (a-c) spheres and cylinders (d-f) with refractive index $n = 1.5$ at varying size parameter q with calculation step size $q = 0.1$. (a) super-resonance mode of sphere, (b) usual jet mode of sphere, (c) whispery gallery mode of sphere (d) usual jet mode of cylinder, (e) strong whispery gallery mode of cylinder (f) weakly excited whispery gallery mode of cylinder. See [Visualization 1](#) and [Visualization 2](#) for details.

The microsphere superlens technology can be also used in 3D super-resolution imaging [150] by combining it with white-light interferometry. Using this principle, spatially resolved features with a resolution of 50 nm in the lateral dimensions and about 10 nm in the vertical dimension have been experimentally demonstrated without the use of fluorescent dyes [150]. Ultimately, the fundamental limit for optical super resolution follows from the information theory [173], which yields a resolution limit of about $\lambda/10 - \lambda/17$. In fact, the basic physics involved in super resolution is related to the image reconstruction by collection of evanescent waves, somehow similar to what was suggested originally for a perfect lens with a negative refractive index [174].

Finally, let us focus briefly on the case of optical nanoscopy by means of cluster assembled materials. It is well known that such materials can form nanometer scale regular structures [175]. A simple example of such cluster assembled materials would be 2D structures of nanoparticles embedded into a transparent host material (PMMA, PDMS, etc.) [128, 169, 170]. However, last year witnessed the emergence of a promising idea, namely that of shaping more involved, 3D, cluster assembled material. For example, it was shown that is possible to fabricate solid immersion lens from these assemblies (also called metamaterial SIL) where small spherical dielectric nanoparticles were used as building blocks to fabricate

the SIL [142]. This technique includes preparing some specific “colloidal solution” of nanoparticles in a water-immiscible organic solvent, which behave as a plastic solid, capable of being molded into desired 3D shapes. Experimentally, it was demonstrated using 15 nm TiO_2 nanoparticles [142]. Having a refractive index $n = 2.5$, such 15 nm TiO_2 particles are non-resonant in the visible range of the spectrum; the first magnetic dipole resonance arises for a size parameter $q \approx 1.2$, corresponding to particle sizes around 175 nm for 460 nm wavelength illumination. It is also far from Kerker resonance at $q \approx 1.1$. Thus, each particle produces just weak Rayleigh scattering and, thus, the metamaterial formed by their assembly is just expected to behave as a homogeneous material with corresponding refractive index $n = 1.9$, in the frame of effective medium theories. The theoretical analysis presented in¹⁴² reveals that a signal from two point sources propagating into such homogeneous media decays exponentially and most of the evanescent wave energy is lost within 50 nm distance, as expected. However, in dense multiple scattering media the near-field coupling between individual scattering centres can lead, at mesoscopic scales, to an increase of light transport and, thus, the total transmission [176]. Indeed, numerical modelling of a metamaterial media constructed from these, closely packed, 15 nm TiO_2 nanoparticles [142] shows that the evanescent wave interacts with the TiO_2 nanoparticles and turns into a propagating wave, which is able to travel within the composed medium towards the far field. Such metamaterial solid immersion lens produces a sharp image with a super-resolution of, at least, 45 nm under a white-light optical microscope, as shown experimentally in Fig. 20. Similar super resolution has been also reported using ZrO_2 ($n = 2.2$) nanoparticles instead immersed in a polymer matrix [177, 178], and probably even better resolutions can be achieved using post processing with coherent diffractive imaging [179].

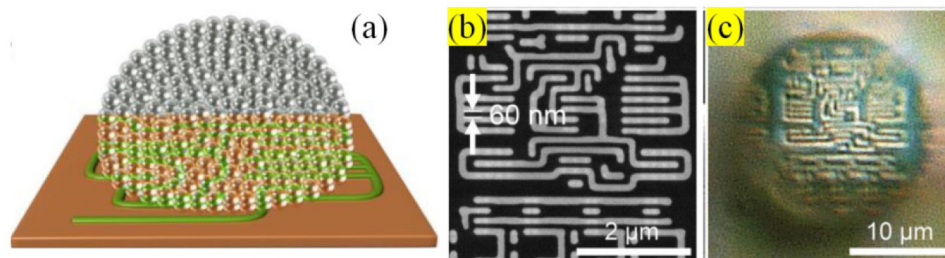


Fig. 20. (a) Schematic depiction of a metamaterial solid immersion lens fabricated from an assembly of TiO_2 particles. (b) SEM image of the test structure, consisting of different shapes and 60 nm pitches. (c) Optical image of the test structure imaged through the metamaterial solid immersion lens using white light [142].

In conclusion, after years of research developments on optical nanoscopy with transparent dielectric particles, it seems that achieving optical resolutions on the level of $\lambda/10$ or even better does not look, any longer, like science fiction. A similar progress has been achieved in understanding and controlling the generation of photonic nanojets with a broad wealth of systems. In this regard, 3D cluster assembled materials have been shown to allow the creation of periodical near field nanojets on the 15-30 nm level [142]. The development of such systems is very promising for nanolithography, as well as for other applications. We have to emphasize that the photonic systems present here (giving rise to either photonic nanojets or nanoscopy devices) are based on materials having a relatively small refractive index contrast with the surrounding media, typically less than two, $n < 2$. As a result, these systems operate in the regime of relatively big size parameter, typically on the order of 10-100 (yielding typically micrometer scale elements in the optical range). This is the main difference with the emergent field of high refractive index photonic systems [180], for which the index contrast $n > 2$ and, thus, may operate in the range of size parameters on the order of unity. This may

be an interesting direction to explore, in which the resonant properties of dielectric particles, and, in particular, the effects of optically excited magnetic modes, may play an interesting role.

Studies of phononic nanojet gave impetus to research in a number of related fields, e.g. in THz range, in plasmonics, acoustic and ultrasound (see e.g. arXiv: 1604.08146 (2016)). Analysis of these activities is outside the scope of this review.

See [Visualization 1](#) and [Visualization 2](#) for photonic nanojet formation, super resonances in sphere and whispering gallery mode in cylinder.

Acknowledgements

The authors B.L and R.P-D are thankful to DSI core fund and A*STAR Science and Engineering Research Council Pharos (grant 1527000025) for support. B.L also acknowledges support by the Russian Ministry of Education and Science (#14.W03.31.0008). I.M and O.M are thankful to Dr. C.-Y. Liu for experimental verification of photonic jet formation in reflection mode. O.M thanks Mendeleev scientific fund of Tomsk State University. Z.W thanks funding support from UK Wales NRN-AEM programme (grants NRN113 and NRNF66). We also acknowledge Arseniy I. Kuznetsov for manuscript reading and edits.